

# 1 Fluid Flow-based Deep Learning (FFDL) for geologic 2 CO<sub>2</sub> Storage

3 Zhen Qin<sup>1</sup>, Yingxiang Liu<sup>2</sup>, Fangning Zheng<sup>1</sup>, Behnam Jafarpour<sup>1\*</sup>

4 <sup>1</sup>Mork Family Department of Chemical Engineering and Materials Science, University of Southern

5 California, 925 Bloom Walk, Los Angeles, 90089, CA, USA

6 <sup>2</sup>Ming Hsieh Department of Electrical and Computer Engineering, University of Southern California, 3740

7 McClintock Avenue, Los Angeles, 90089, CA, USA

## 8 Key Points:

- 9 • **Novel and generic approach:** Physics-encoded model to predict the evolution  
10 of pressure and saturation fields during geologic CO<sub>2</sub> storage under dynamic in-  
11 jection rates and permeability variations
- 12 • **Physics-encoded architecture:** A novel architecture featuring a fluid flow physics-  
13 based encoder and a residual-based processor.
- 14 • **Physics-based operator:** A novel nonlinear activation function, the physics-based  
15 operator, is applied to capturing physical relationships.
- 16 • **Generalization and extrapolation:** Robust generalizable approach with ac-  
17 curate predictions over extended time frames and strong extrapolation capabil-  
18 ities.

---

\*Corresponding author

Corresponding author: Behnam Jafarpour, behnam.jafarpour@usc.edu

19      **Abstract**

20      Carbon capture and storage (CCS) is one of the few strategies for reducing CO<sub>2</sub> emis-  
 21      sions by injecting it into deep geologic formations. The injection of CO<sub>2</sub> into heteroge-  
 22      neous rock formations triggers a set of complex coupled flow and transport processes that  
 23      are not trivial to describe and predict. Advanced numerical simulation is often used as  
 24      a standard tool to predict the spatial-temporal evolution of the CO<sub>2</sub> plume and the in-  
 25      duced pressure changes. However, numerical simulation is computationally demanding  
 26      and can limit the use of standard field management workflows, such as risk assessment  
 27      workflows, and hinder real-time analysis and decision-making for risk mitigation. Stan-  
 28      dard deep learning models provide powerful alternative prediction tools. However, they  
 29      also have important limitations, including lack of interpretability, extensive data needs,  
 30      and physical inconsistency.

31      To overcome these limitations, a Fluid Flow-based Deep Learning (FFDL) archi-  
 32      tecture is presented for spatial-temporal prediction of the injected CO<sub>2</sub> in storage for-  
 33      mations. The architecture of FFDL consists of a physics-based encoder to construct phys-  
 34      ically meaningful latent variables, and a residual-based processor to predict the evolu-  
 35      tion of the state variables. The FFDL model uses physical operators that serve as non-  
 36      linear activation functions and impose hard constraints to respect the general structure  
 37      of the fluid flow equations. A comprehensive investigation of FFDL, based on a field-scale  
 38      saline aquifer, is used to demonstrate its superior performance compared to standard deep  
 39      learning models. The results show that FFDL exhibits strong generalization capability  
 40      and provides more reliable and physically consistent predictions of CO<sub>2</sub> plume migra-  
 41      tion. The flexibility of FFDL makes it suitable for various applications, including decision-  
 42      making, optimization, and inverse modeling.

43      **1 Introduction**

44      Carbon capture and storage (CCS) is an important component in reducing the CO<sub>2</sub>  
 45      emissions by capturing from point sources and injecting it into deep geologic formations.  
 46      Although geologic CO<sub>2</sub> storage has significant potential, it is still in the early stages. Con-  
 47      cerns about CO<sub>2</sub> migration or leakage into shallow aquifers call for robust monitoring  
 48      and risk management technologies (Zheng et al., 2022, 2021; Celia et al., 2015). While  
 49      current monitoring methods can track the movement of the injected CO<sub>2</sub> plume, accu-  
 50      rately quantifying its volume and migration path remains a challenge for monitoring and  
 51      verification purposes (Bui et al., 2018). Moreover, predicting the dynamics of pressure  
 52      buildup and CO<sub>2</sub> migration is essential for guiding decision-making (Zheng et al., 2021)  
 53      and for assessing real-time risks throughout the life cycle of a project (Ajayi et al., 2019).

54      Reliable prediction of the CO<sub>2</sub> plume migration often requires spatial and tempo-  
 55      ral analysis, potentially involving detailed simulation models. The injection of CO<sub>2</sub> into  
 56      subsurface formations triggers a complex multi-component, multiphase flow system. The  
 57      complex relationships involving miscibility, capillary pressure, and relative permeabil-  
 58      ity, as well as coupled physics lead to nonlinear coupled systems of partial differential  
 59      equations (PDEs) that are not trivial to solve (Bandilla et al., 2015). Furthermore, field-  
 60      scale geologic CO<sub>2</sub> storage (GCS) projects span extensive spatial and temporal scales,  
 61      including both injection and post-injection periods (Ajayi et al., 2019; X. Jiang, 2011).  
 62      Therefore, numerical simulation for GCS at the field scale can become computationally  
 63      prohibitive, particularly for complex tasks such as optimization and uncertainty quan-  
 64      tification. Another significant challenge is estimating the time-varying storage capacity  
 65      of the geologic formations, which is influenced by geologic conditions, injectivity and field  
 66      development plans (Gorecki et al., 2015). Accurate quantification of uncertainty and po-  
 67      tential risks typically involves multiple simulation runs, which can impede the implemen-  
 68      tation of real-time analysis and risk assessments in GCS projects. Consequently, there  
 69      is a growing need for innovative approaches that can provide accurate and efficient real-

70 time monitoring and forecasting of CO<sub>2</sub> plume migration and pressure buildup during  
 71 GCS operations.

72 In recent years, deep learning (DL)-based approaches have emerged as promising  
 73 alternatives to traditional numerical simulations for predicting the spatial-temporal evo-  
 74 lution of fluid dynamics in the subsurface. Specifically, convolutional neural networks  
 75 (CNNs) that have demonstrated a strong capability for processing image data have found  
 76 widespread application in predicting the spatial and temporal evolution of subsurface  
 77 flow systems. Zhu and Zabaras (2018) proposed a fully convolutional encoder-decoder  
 78 architecture to approximate the mapping from permeability to pressure and velocity maps  
 79 for a 2-dimensional steady-state Darcy flow problem. Mo, Zhu, et al. (2019) extended  
 80 the work in Zhu and Zabaras (2018) to predict the responses from a dynamic multiphase  
 81 flow problem at different time steps. Y. Wang and Lin (2020) designed a custom archi-  
 82 tecture tailored for single- and two-phase flow systems, incorporating sparsely connected  
 83 layers to account for the inherent sparse input-output interaction.

84 Among the family of CNNs, U-Net (Ronneberger et al., 2015) was originally de-  
 85 signed for biomedical image segmentation and has emerged as a mainstream model for  
 86 prediction tasks in the subsurface domain (Wen, Tang, & Benson, 2021; Z. Jiang et al.,  
 87 2021; H. Tang et al., 2021; Yan, Harp, Chen, & Pawar, 2022). U-Net excels in captur-  
 88 ing complex patterns by retaining multi-scale details of input images through skip con-  
 89 nections. This feature of U-Net facilitates the integration of high-resolution details, re-  
 90 duces the search space of model parameters, and mitigates the gradient vanishing issue  
 91 often encountered in deep architectures. Yan, Harp, Chen, and Pawar (2022) proposed  
 92 a physics-constrained smoother to enhance the pressure prediction generated by U-Net.  
 93 Their approach incorporates the time step as an additional input, allowing the U-Net  
 94 model to predict pressure or saturation at different time steps. This method does not  
 95 explicitly capture the dynamics of the flow system. Instead, it approximates a static map-  
 96 ping conditioned on the time step. Alternatively, spatial-temporal predictions can also  
 97 be achieved using auto-regressive architecture (Mo, Zabaras, et al., 2019; Z. Jiang et al.,  
 98 2021), recurrent architecture (M. Tang et al., 2020) or by jointly predicting all time frames  
 99 (Wen, Hay, & Benson, 2021; Wen et al., 2022, 2023). M. Tang et al. (2020) introduced  
 100 a combined model called Recurrent R-U-Net that integrates Residual U-Net (R-U-Net)  
 101 (Wen, Tang, & Benson, 2021) with convolutional long short-term memory (ConvLSTM)  
 102 network (Shi et al., 2015) to capture the evolution of saturation and pressure in the 2D  
 103 two-phase waterflooding problem. This combined architecture was later extended to ad-  
 104 dress 3D flow problems in waterflooding (M. Tang et al., 2021) and CO<sub>2</sub> sequestration  
 105 (M. Tang et al., 2022). Different from the recurrent architecture, Wen et al. (2023) pro-  
 106 posed a nested framework of DL models for 4D spatial-temporal prediction of pressure  
 107 and saturation in a joint way by utilizing Fourier Neural Operator (FNO) (Li et al., 2020).  
 108 Their methodology involves dividing a large reservoir into multiple scales (levels), with  
 109 each level employing an FNO model to predict either pressure or saturation. By com-  
 110 bining the FNOs of each level sequentially, the states of the entire reservoir can be pre-  
 111 dicted. Unlike the recurrent nature of ConvLSTM, the FNO approach predicts all time  
 112 steps simultaneously, enabling parallelized prediction across the time domain. However,  
 113 the FNO's 4D architecture results in a significantly larger number of trainable param-  
 114 eters, with approximately 80 to 150 million parameters for each level, making it com-  
 115 putationally demanding and potentially resource-intensive when extending it to more  
 116 complex problems.

117 Despite the demonstrated effectiveness of DL models, the approaches mentioned  
 118 above have limitations and are tailored to specific scenarios. Notably, in GCS projects  
 119 that can span decades for injection and potentially much longer for the post-injection  
 120 period, the predictive model's capability and flexibility to forecast over arbitrary time  
 121 frames are crucial. However, existing DL models are constrained to predicting within fixed  
 122 periods and encounter challenges in long-term predictions (which require extrapolating

power). Deep learning models have limited extrapolation power and do not provide reliable predictions beyond the data distribution defined by the training set (Willard et al., 2022), leading to the out-of-distribution (OOD) generalization problem. As reflected in Mo, Zhu, et al. (2019), the prediction over the OOD time steps becomes an extrapolation task that can challenge deep learning models, as the saturation predictions during the extrapolation may become physically inconsistent. This is particularly important for GCS projects that require long-term prediction horizons. Another important feature is the flexibility of the model in terms of providing predictions over different development scenarios. For instance, the models should be able to capture the response of the storage formations to time-varying controls, which is important in optimizing the performance of the field by dynamically managing the injection strategies based on the in-situ reservoir conditions and monitoring data (Pawar et al., 2015).

To enhance predictive capabilities and overcome limitations, an emerging and active research field focuses on integrating physical principles and domain knowledge into neural networks (NNs) (Willard et al., 2022; Faroughi et al., 2023). A flexible approach is to incorporate governing equations into the loss function to constrain the neural networks during training, known as Physics-informed Neural Networks (PINNs) (Raissi et al., 2019). The PINN framework offers a flexible implementation across various physical systems and has found successful applications in the subsurface domains (N. Wang et al., 2020; Shokouhi et al., 2021; Yan, Harp, Chen, Hoteit, & Pawar, 2022). However, physics-informed approaches often struggle with adhering to boundary conditions, as they implement physical constraints in a "soft" manner. Furthermore, the inherent complexity of multiphase flow in heterogeneous porous media presents challenges in implementing the closed-form residuals of nonlinear PDEs as loss functions (Yan, Harp, Chen, Hoteit, & Pawar, 2022). The training of deep learning models using physics-informed loss functions without labeled data can be affected by the complexity and nonlinearity of the integrated physics. The presence of complex governing equations can lead to highly nonlinear and non-convex loss functions, complicating the training process (Fuks & Tchelepi, 2020). These issues may challenge the use of data-free approaches in more complex problems, including high-dimensional and highly nonlinear systems (Cuomo et al., 2022; Muther et al., 2023).

Another fit-for-purpose alternative involves hard-encoding the underlying physics into the architecture of neural networks, endowing the resulting models with an inductive bias tailored to specific physical problems (Faroughi et al., 2023; Karniadakis et al., 2021). In contrast to physics-informed approaches, physics-encoded architectures impose hard constraints. By capturing the underlying physical dependencies among variables, these architectures demonstrate their connections to Ordinary Differential Equations (ODEs) (E, 2017; E et al., 2017; Lu et al., 2018) and PDEs (Long et al., 2018, 2019; Ruthotto & Haber, 2020; Rao et al., 2021). Long et al. (2018, 2019) proposed PDE-Net to learn PDEs from data. In their work, the CNN is combined with Residual Network (ResNet) (He et al., 2016) to approximate the evolution of PDE with the forward Euler as the temporal discretization. Rao et al. (2021) introduced the product block to emulate the governing terms in PDEs. Their study utilizes convolutional layers to learn spatial dependencies and employs a recurrent form of ResNet for approximating temporal evolution. The resulting DL model has shown good performance in extrapolation tasks. More recently, Dulny et al. (2022) proposed NeuralPDE to combine Neural Ordinary Differential Equations (NeuralODEs) (Chen et al., 2018) with the Method of Lines (MOL) using CNNs to approximate the spatial component in PDEs. They state that CNNs can approximate the MOL, a numerical method of solving time-dependent PDEs by representing them as systems of ODEs through spatial discretization. Nonetheless, these studies tend to simplify the governing equations and approximate the dynamics in an explicit form.

In this study, we propose a novel physics-encoded DL model, named Fluid Flow-based Deep Learning (FFDL), for predicting the spatial-temporal evolution of the pressure and saturation in geologic CO<sub>2</sub> storage. To bridge the gaps in the existing models, the FFDL model is designed to handle time-varying well controls and to provide long-term predictions. The architecture of FFDL primarily comprises a physics-based encoder for constructing physically meaningful latent variables, a residual-based processor for the recurrent prediction of latent variables, a control encoder for constructing a latent representation of sink or source term, and a decoder for approximating the mapping from latent variables to outputs, namely pressure and saturation. The physics-based encoder, along with the control encoder, can construct different governing terms in the PDEs for multiphase flow, including accumulation, advection, and sink/source terms. Similar to the work in (Long et al., 2019; Rao et al., 2021; Dulny et al., 2022), the convolutional layers are employed to capture the spatial dependencies. However, our model extends beyond these by 1) introducing physics-based operators as the activation functions, 2) constructing latent representations of the governing terms to better approximate the dynamics, and 3) updating the latent governing terms in a coupled and implicit form. We also present a modified Recurrent R-U-Net, based on the work in M. Tang et al. (2022), as a baseline model due to its similar architecture and capability for extension to time-varying control and arbitrary time steps. The predictive performance of FFDL is investigated using a field-scale model of GCS in a saline aquifer. Our results show that FFDL outperforms the Recurrent R-U-Net on test sets featuring unseen permeability, well controls, and time frames.

The remaining sections of this paper are organized as follows. Section 2 presents the problem statement for the spatial-temporal prediction task and introduces the architectures of the proposed physics-based encoder and residual-based processor. In Section 3, we provide a brief overview of the experimental setups and describe the modifications made to Recurrent R-U-Net. The experimental results and discussions are presented in Section 4. Finally, Section 5 offers conclusions on this work and highlights the advantages of the proposed model.

## 2 Methodology

### 2.1 Problem Statement

This study addresses a spatial-temporal prediction task governed by a set of coupled PDEs within a 3D reservoir composed of grid blocks  $\mathcal{D} \subset \mathbb{R}^3$ . The prediction task can be formulated as  $\mathbf{X} = \mathcal{F}(\mathbf{x}^t, \mathbf{m}, \mathbf{U})$ , given the inputs  $\mathbf{x}^t$  as the dynamic states at time step  $t$ ,  $\mathbf{m}$  as parameters, and  $\mathbf{U}$  as future controls. The output sequence  $\mathbf{X} = \{\mathbf{x}^{t+1}, \mathbf{x}^{t+2}, \dots\}$  represents the dynamic variables over the subsequent time steps, and the operator  $\mathcal{F}$  denotes the mapping from inputs to outputs. For each coordinate  $\omega \in \mathcal{D}$ , the dynamic variable  $\mathbf{x}^t(\omega)$  at time step  $t$  consists of pressure  $\mathbf{p}^t(\omega) \in \mathbb{R}$  and saturation of non-wetting phase  $\mathbf{S}_n^t(\omega) \in \mathbb{R}$ . The input parameters  $\mathbf{m}(\omega) \in \mathbb{R}^{d_m}$  characterize the model parameters, such as permeability, porosity, grid volume, and elevation, at point  $\omega$ . The control sequence  $\mathbf{U} = \{\mathbf{u}^{t+1}, \mathbf{u}^{t+2}, \dots\}$  denotes well controls over future time steps. At any given step  $t$ , the control variable  $\mathbf{u}^t$  can be the bottom-hole pressure (BHP) or flow rate. The value of each grid cell  $\mathbf{u}^t(\omega) \in \mathbb{R}^{d_u}$  corresponds to the control value (e.g., injection rate) at a well location  $\omega$  and is zero if the cell does not contain a well. Superscripts  $d_x$ ,  $d_m$ , and  $d_u$  indicate the dimensions of dynamic states, input parameters, and control variables at a point  $\omega$ , respectively. The goal of this work is to approximate the operator  $\mathcal{F}$  with the proposed deep learning model  $\mathcal{F}_\theta$ , where  $\theta$  represents the trainable parameters. In this paper, variables denoted in bold represent high-dimensional tensors, while those not in bold refer to scalars. For brevity, we primarily focus on the dimensionality of high-dimensional tensors at individual spatial points  $\omega$ , rather than the entire spatial domain.

In this approach, we avoid the direct learning of the pressure and saturation dynamics. Instead, we convert these variables into physically meaningful latent variables and learn the dynamics in latent space. The latent representation  $\mathbf{z}^t = \{\mathbf{z}_{acc}^t, \mathbf{z}_{adv}^t, \mathbf{z}_{src}^t\}$  consists of three components representing the accumulation, advection, and sink/source terms of the governing PDEs in the latent space, respectively. As depicted in Figure 1, the proposed deep learning model mainly consists of the encoder, processor, control encoder, and decoder modules. Initially, the encoder predicts the first two latent variables over the next time step,  $\mathbf{z}_{acc}^{t+1}$  and  $\mathbf{z}_{adv}^{t+1}$ , using  $\mathbf{x}^t$  and  $\mathbf{m}$  as inputs. Concurrently, the control encoder produces the latent variables  $\mathbf{z}_{src}^{t+1}$  given the control variables  $\mathbf{u}^{t+1}$ . The processor receives three latent variables as input and generates the updated latent variables  $\mathbf{z}_{acc}^{t+1}$  and  $\mathbf{z}_{adv}^{t+1}$  as outputs. These outputs are then sent to 1) the decoder for the prediction of the dynamic variables  $\mathbf{x}^{t+1}$ , and to 2) the processor itself for the estimation of the new latent variables  $\mathbf{z}_{acc}^{t+2}$  and  $\mathbf{z}_{adv}^{t+2}$ . The decoder takes the updated latent variables  $\mathbf{z}_{acc}^{t+1}$  and  $\mathbf{z}_{adv}^{t+1}$ , as well as the static variable  $\mathbf{m}$ , as inputs. By including  $\mathbf{m}$ , the decoder is designed to decouple the effects of parameters from the latent variables, functioning as the inverse of the encoder. In a recurrent manner, the processor utilizes the previous latent variables as initial estimations and updates them for the next time step by integrating  $\mathbf{z}_{src}^{t+1}$  as external inputs. To articulate the model's function, the process  $\mathbf{X} = \mathcal{F}(\mathbf{x}^t, \mathbf{m}, \mathbf{U})$  can be modularized as follows:

$$\begin{aligned} \{\mathbf{z}_{acc}^{t+1}, \mathbf{z}_{adv}^{t+1}\} &= \mathcal{F}_{\theta_{InputToLatent}}(\mathbf{x}^t, \mathbf{m}), \\ \{\mathbf{z}_{src}^{t+n}\} &= \{\mathcal{F}_{\theta_{ControlToLatent}}(\mathbf{u}^{t+n})\}, n = 1, 2, \dots, \\ \{\mathbf{z}_{acc}^{t+n}, \mathbf{z}_{adv}^{t+n}\} &= \{\mathcal{F}_{\theta_{LatentToLatent}}(\mathbf{z}_{acc}^{t+n}, \mathbf{z}_{adv}^{t+n}, \mathbf{z}_{src}^{t+n})\}, n = 1, 2, \dots, \\ \{\mathbf{x}^{t+n}\} &= \{\mathcal{F}_{\theta_{LatentToOutput}}(\mathbf{z}_{acc}^{t+n}, \mathbf{z}_{adv}^{t+n}, \mathbf{m})\}, n = 1, 2, \dots, \end{aligned} \quad (1)$$

where, the operators  $\mathcal{F}_{\theta_{InputToLatent}}$ ,  $\mathcal{F}_{\theta_{ControlToLatent}}$ ,  $\mathcal{F}_{\theta_{LatentToLatent}}$ , and  $\mathcal{F}_{\theta_{LatentToOutput}}$  represent the encoder, control encoder, processor, and decoder modules, respectively.

## 2.2 Physics-Encoded Deep Learning Model

One of the main contributions of this work is the design of the encoder and processor modules, as depicted in Figure 2. In contrast, the control encoder and decoder are implemented using standard convolutional layers with simpler configurations. This subsection delineates 1) the physical operators used in the encoder, and 2) the detailed architectures of the encoder and processor. A comprehensive description of the governing equations for geologic CO<sub>2</sub> storage is provided in Appendix A. The explanation of the control encoder and decoder is provided in Appendix B.

In our model, the encoder is designed to capture the relationship between the latent representations of the governing terms (i.e., accumulation and advection) and various input variables (e.g., pressure, saturation, permeability, etc.) using physical operators. Recent works designed neural operators to either 1) construct the latent variables in the spectral domain (Li et al., 2020; Wen et al., 2022; Xiong et al., 2023) or 2) introduce high-frequency features to the DL model (H. Wu et al., 2023). Although these advanced architectures effectively address the issue of spectral bias (Tancik et al., 2020; Rrahaman et al., 2019), the constructed latent variables lack interpretability, resulting in a black-box architecture. In contrast, we adopt the concept of physical operators to map the input variables to physically meaningful latent variables that represent accumulation and advection terms. This design is inspired by the Operator-Based Linearization (OBL) approach (Voskov, 2017), which represents the governing terms as combinations of operators and linearizes them within the parameter space (pressure, saturation, and component) to facilitate the application of numerical solvers.

Two primary motivations underpin the transition from input variables to physics-based latent representations. First, the governing equations of the system involve implicit and nonlinear dependencies on pressure and saturation, challenging the derivation of explicit update forms. Previous studies have utilized ResNet (or skip connections) for

direct updates of variables in explicit form. These methods often rely on simplifications of PDEs (J. Nagoor Kani & Elsheikh, 2019; Y. Wang & Lin, 2020) or are tailored to specific problem characteristics (Rao et al., 2021). In contrast to direct updates of dynamic variables, our method focuses on the dynamics within the latent space by mapping them onto physics-based latent variables. This design circumvents the assumptions required by previous works, offering a more thorough treatment of the underlying physics. Second, predicting the dynamics within the latent space offers our model flexibility and generalizability. The physics-based encoder can flexibly adapt to various physical terms, such as capillary and gravity terms, through the design of physics-based operators. Moreover, the physical operators enable our model to effectively generalize across diverse input variables and learn the physical relationship between diverse inputs and outputs. Consequently, this design potentially extends the applicability of our model to various tasks and scenarios.

### 2.2.1 Physical Operators

For geologic CO<sub>2</sub> sequestration sites, such as saline aquifers, the system consists of two primary phases: a water-rich phase and a CO<sub>2</sub>-rich phase. In this work, we simplify the CO<sub>2</sub>-brine system to an immiscible two-fluid-phase system with no internal component gradient. As a result, the mass balance equation can be written in terms of phase-based balance equations:

$$\frac{\partial}{\partial t} (\phi S_\xi \rho_\xi) + \nabla \cdot (\rho_\xi \mathbf{v}_\xi) = \rho_\xi \tilde{q}_\xi, \quad \xi \in \{w, n\}, \quad (2)$$

where  $\phi$  is the porosity;  $S_\xi$  and  $\rho_\xi$  are the saturation and density of phase  $\xi$ , respectively;  $\mathbf{v}_\xi$  is the volumetric flux vector for phase  $\xi$ ;  $\tilde{q}_\xi$  is external sources or sinks of volumetric rate per unit volume of phase  $\xi$ . The phase  $\xi$  is  $n$  for the non-wetting phase (super-critical CO<sub>2</sub>) and  $w$  for the wetting phase (brine).

We rewrite the Eq. 2 as a combination of operators in an algebraic form for the whole reservoir in three-dimensional space  $\mathcal{D}$ :

$$\mathbf{r}_\xi(\mathbf{x}, \mathbf{m}, \mathbf{u}) = (\mathbf{z}_{acc,\xi}(\mathbf{x}) - \mathbf{z}_{acc,\xi}(\mathbf{x}^{t-1})) - \mathbf{z}_{adv,\xi}(\mathbf{x}, \mathbf{m}) + \mathbf{z}_{src,\xi}(\mathbf{x}, \mathbf{u}) = \mathbf{0}, \quad (3)$$

where  $\mathbf{r}_\xi$  is the residual of the governing equation for phase  $\xi$  over the entire reservoir;  $\mathbf{z}_{acc,\xi}$ ,  $\mathbf{z}_{adv,\xi}$ , and  $\mathbf{z}_{src,\xi}$  are the accumulation, advection, and sink/source terms for phase  $\xi$ , respectively.

The governing terms are calculated through the physical operators. Detailed derivation of the governing equations and operators are provided in Appendix A. Here, we define the operators as follows

$$\mathbf{z}_{acc,\xi}(\mathbf{x}) = \mathbf{c}_\phi \circ \mathbf{S}_\xi \circ \rho_\xi = (1 + \mathbf{c}_r \circ (\mathbf{p} - \mathbf{p}_{ref})) \circ \mathbf{S}_\xi \circ \rho_\xi, \quad (4)$$

$$\mathbf{z}_{adv,\xi}(\mathbf{x}, \mathbf{m}) = \mathbf{a}(\mathbf{m}) \circ \sum_l \beta_{\xi,l}(\mathbf{x}) \circ \mathbf{b}_l(\mathbf{x}, \mathbf{m}), \quad (5)$$

$$\mathbf{z}_{src,\xi}(\mathbf{x}, \mathbf{u}) = \mathbf{a}(\mathbf{m}) \circ \rho_\xi \circ \mathbf{q}_\xi = \mathbf{a}(\mathbf{m}) \circ \rho_\xi \circ \mathbf{V} \circ \tilde{q}_\xi, \quad (6)$$

$$\mathbf{a}(\mathbf{m}) = \Delta t \mathbf{I}_{PV}, \quad (7)$$

$$\beta_{\xi,l}(\mathbf{x}) = \boldsymbol{\lambda}_\xi \circ \rho_\xi, \quad (8)$$

$$\mathbf{b}_l(\mathbf{x}, \mathbf{m}) = \mathbf{T}_m^l \circ \Delta \psi_\xi^l = \mathbf{T}_m^l \circ (\psi_\xi^v - \psi_\xi^u), \quad (9)$$

where the symbol  $\circ$  represents the Hadamard product (or element-wise production);  $\mathbf{c}_\phi$  is defined as an update multiplier for the initial porosity;  $\mathbf{c}_r$ ,  $\mathbf{p}_{ref}$ , and  $\mathbf{V}$  are rock compressibility, reference pressure, and grid volume, respectively;  $\mathbf{q}_\xi$  is the volumetric flow rate for phase  $\xi$ ;  $\Delta t$  is a scalar and represents the time interval;  $\mathbf{I}_{PV}$  is the inverse of the

initial pore volume of a grid cell  $\phi_0 V$ ;  $\lambda_\xi$  is the mobility of phase  $\xi$ ;  $\mathbf{T}_m^l$  is the geometric part of the transmissibility of interface  $l$  between two grids  $u$  and  $v$ ;  $\Delta\psi_\xi^l$  is the phase potential difference between the two grid cells  $u$  and  $v$ , of which the phase potentials are  $\psi_\xi^u$  and  $\psi_\xi^v$ , respectively. For the design of the encoder, the phase potential is simplified by neglecting the capillary pressure and represented as  $\psi_\xi = \mathbf{p} + \rho_\xi \circ \mathbf{D}$ . The variable  $\mathbf{D} = g \mathbf{d}$  refers to the gravity term defined as the product of the gravitational acceleration ( $g$ ) and the elevation (or depth) of grid cells ( $\mathbf{d}$ ). The parameter  $\mathbf{m}$  is defined as a set of three components  $\{\mathbf{T}_m, \mathbf{I}_{PV}, \mathbf{D}\}$ .

### 316 2.2.2 Physics-based Encoder

317 The encoder consists of three stages in a sequence (See Figure 2 (a)). The first stage  
 318 of the encoder takes the dynamic variables  $\mathbf{x}$  and parameter  $\mathbf{m}$  as inputs. The output  
 319 from the first stage is a set of physical features  $\mathbf{f}$  used in the operators and defined as  
 320 follows:

$$\mathbf{f} = \{c_\phi, \rho_\xi, \lambda, \Delta\mathbf{p}, \Delta(\rho_\xi \circ \mathbf{D})\}. \quad (10)$$

321 The dependencies of  $c_\phi$  and  $\rho_\xi$  on pressure and the dependency of  $\lambda_\xi$  on pressure  
 322 and saturation are parameterized using fully-connected (FC) NN, which is named state-  
 323 related operator (Figure 3 (a)). In this work, we parameterize the state-related opera-  
 324 tor using a two-layer fully connected NN with the hidden unit  $d_o$ . The Gaussian Error  
 325 Linear Unit (GELU) (Hendrycks & Gimpel, 2023) serves as the nonlinear activation func-  
 326 tion after each layer. Features  $\Delta\mathbf{p}$  and  $\Delta(\rho_\xi \circ \mathbf{D})$  are the differential pressure and grav-  
 327 ity terms used in the potential difference  $\Delta\psi$ , which are calculated through the spatial-  
 328 related operator (Figure 3 (b)). In a structured grid system,  $\mathbf{p}$  and  $\mathbf{D}$  are first padded  
 329 with reflection padding around the edges of tensors, which serves as a closed boundary.  
 330 Given the padded terms,  $\Delta\mathbf{p}$  and  $\Delta(\rho_\xi \circ \mathbf{D})$  are computed along the  $x$ -,  $y$ -, and  $z$ -directions.  
 331 The differential operator is implemented by applying the discretization stencil  $\frac{1}{2} \times [-1, 0, 1]$   
 332 along each of the three directions.

333 In the second stage, convolutional layers are used to project all the components of  
 334 dynamic variable  $\mathbf{x}$ , input parameters  $\mathbf{m}$ , and physical feature  $\mathbf{f}$  into a high-dimensional  
 335 hidden feature  $\mathbf{h}$ . Each component of the hidden feature  $\mathbf{h}$  has a dimensionality of  $d_h$   
 336 at the point  $\omega$ . Hidden features are then passed to the operator blocks defined in Eqs.  
 337 (4 - 9). The operator blocks return the high-dimensional representations of the accumu-  
 338 lation and advection terms. The goal of extending the feature dimensionality before the  
 339 operator blocks is to project the physical relationships in a high-dimensional space. In-  
 340 stead of applying nonlinear functions, the Hadamard product is used to introduce non-  
 341 linearity in the encoder.

342 In the third stage, we further map the accumulation and advection terms into a  
 343 high-dimensional latent space with the dimension of  $d_l$  ( $d_l > d_h$ ). Simultaneously, the  
 344 latent variables are downsampled through the convolutional layers, reducing the spatial  
 345 dimension by a factor of 2. The outputs of this stage are the latent variables  $\mathbf{z}_{acc}^t$  and  
 346  $\mathbf{z}_{adv}^t$ . The downsampling is employed to increase the receptive field of the convolutional  
 347 layers while reducing the GPU memory demand.

348 While the notation of latent variables does not specify the fluid phase, the latent  
 349 variables are computed separately for the wetting and non-wetting phases and then con-  
 350 catenated. As a result, each latent variable sent to the next layer encompasses the la-  
 351 tent representations for the two phases. As shown in Figure 2 (a), the dynamic input  
 352  $\mathbf{x}$  is defined for the previous time step  $t-1$ , while the latent variable  $\mathbf{z}$  corresponds to  
 353 the current time step  $t$ . Therefore, the purpose of the encoder is to generate an initial  
 354 estimate of the latent variables for time step  $t$ . These latent variables will be further up-  
 355 dated by the processor, taking into account the external effect of the control variable.

356 The encoder  $\mathcal{F}_{\theta_{\text{InputToLatent}}}$  can then be decomposed into three stages as follows:

$$\begin{aligned} \mathbf{f} &= \mathcal{F}_{\theta_{\text{InputToFeature}}}(\mathbf{x}, \mathbf{m}), \\ \mathbf{h} &= \mathcal{F}_{\theta_{\text{FeatureToHidden}}}(\mathbf{f}, \mathbf{x}, \mathbf{m}), \\ \{\mathbf{z}_{\text{acc}}, \mathbf{z}_{\text{adv}}\} &= \mathcal{F}_{\theta_{\text{HiddenToLatent}}}(\mathbf{h}), \end{aligned} \quad (11)$$

357 where  $\mathcal{F}_{\theta_{\text{InputToFeature}}}$ ,  $\mathcal{F}_{\theta_{\text{FeatureToHidden}}}$ , and  $\mathcal{F}_{\theta_{\text{HiddenToLatent}}}$  refer to the three stages of the  
 358 physics-based encoder, respectively. The dimensions  $d_o$ ,  $d_h$ , and  $d_l$  in these three stages  
 359 are the hyperparameters defined by users. The selection of these hyperparameters and  
 360 their feasible ranges are provided in Appendix B.

361 Neural networks parameterize the state-related operator in the first stage with  $d_o$   
 362 hidden units and learn the nonlinear dependencies with complicated formulas, such as  
 363 Equation of State (EoS). In contrast to the parameterization of the state-related oper-  
 364 ator, the spatial and physical operator blocks are non-parametric and serve as hard con-  
 365 straints to enforce adherence to the underlying physics.

### 366 2.2.3 Residual-based Processor

367 The processor is implemented as a variant of recurrent neural network (RNN) with  
 368 a customized recurrent unit, as illustrated in Figure 2 (b). The inputs to the processor  
 369 are the governing terms in the latent space  $\mathbf{z}^t$  to represent the accumulation  $\mathbf{z}_{\text{acc}}^t$ , ad-  
 370 vection  $\mathbf{z}_{\text{adv}}^t$ , and sink/source  $\mathbf{z}_{\text{src}}^t$  for wetting and non-wetting phases. The latent rep-  
 371 resentation of the sink/source term comes from the control encoder  $\mathcal{F}_{\theta_{\text{ControlToLatent}}}$ . Each  
 372 customized recurrent unit, also referred to as a processor block, consists of  $N_{rl}$  residual  
 373 layers that iteratively update the latent variables  $\mathbf{z}_{\text{acc}}^t$ ,  $\mathbf{z}_{\text{adv}}^t$ , and  $\mathbf{z}_{\text{src}}^t$ , where  $N_{rl}$ , de-  
 374 notes the number of residual layers. To make the proposed model more memory-efficient  
 375 and to increase the receptive field of the convolutional kernel, we further reduce the spa-  
 376 tial dimension of the latent variables  $\mathbf{z}_{\text{acc}}^t$ ,  $\mathbf{z}_{\text{adv}}^t$ , and  $\mathbf{z}_{\text{src}}^t \in \mathbb{R}^{\mathcal{D} \times d_l}$  by a factor of 2 and  
 377 simultaneously project them onto the feature space with a higher dimensionality of  $d_r$   
 378 ( $d_r > d_l$ ). The resulting latent features are used to calculate the residual term  $\delta\mathbf{z}^t$ , which  
 379 is then projected back to the original dimension  $\mathcal{D} \times d_l$  and added to the latent vari-  
 380 able  $\mathbf{z}^t$ .

381 The residual layer updates the latent variables based on the concept of the resid-  
 382 ual for governing equations. For a numerical solver, the Newton-Raphson method is com-  
 383 monly applied, which is written as:

$$\mathbf{J}(\mathbf{x}^k)(\mathbf{x}^{k+1} - \mathbf{x}^k) = -\mathbf{r}(\mathbf{x}^k), \quad (12)$$

384 where  $\mathbf{J}$  is the Jacobian matrix at the inner iteration step  $k$  of the nonlinear solver;  $\mathbf{r}(\mathbf{x}^k)$   
 385 denotes the residual of the governing equations for iteration  $k$ .

386 In this study, the design of the processor is inspired by the Newton-Raphson method.  
 387 Instead of iteratively updating the dynamic variable  $\mathbf{x}^k$ , we update the latent variables  
 388 and parameterize the update procedure using neural networks. First, we rewrite the Eq.  
 389 (12) as follows:

$$\begin{aligned} \delta\mathbf{x}^k &= \mathbf{x}^{k+1} - \mathbf{x}^k = -\left(\mathbf{J}^k\right)^{-1}\mathbf{r}^k \\ &\approx \mathcal{F}(\mathbf{r}^k, \mathbf{x}^k) \approx \mathcal{F}_{\theta_{\text{ResidualToDiff}}}(\mathbf{r}^k, \mathbf{z}^k). \end{aligned} \quad (13)$$

390 The dependency of input difference  $\delta\mathbf{x}^k$  on terms  $\mathbf{x}^k$  and  $\mathbf{r}^k$  is parameterized by  
 391 the operator  $\mathcal{F}_{\theta_{\text{ResidualToDiff}}}$ . To further facilitate the update, we introduce another op-  
 392 erator  $\mathcal{F}_{\theta_{\text{DiffToDiff}}}$  to convert the difference  $\delta\mathbf{x}^k$  to the latent space, which is shown as fol-  
 393 lows:

$$\delta\mathbf{z}^k = \mathbf{z}^{k+1} - \mathbf{z}^k \approx \mathcal{F}_{\theta_{\text{DiffToDiff}}}(\delta\mathbf{x}^k), \quad (14)$$

394 where  $\mathcal{F}_{\theta_{\text{DiffToDiff}}}$  approximates the mapping between the input difference  $\delta \mathbf{x}^k$  and the  
 395 latent difference  $\delta \mathbf{z}^k$ . Finally,  $\delta \mathbf{z}^k$  can be written as:

$$\delta \mathbf{z}^k = \mathcal{F}_{\theta_{\text{DiffToDiff}}}(\mathcal{F}_{\theta_{\text{ResidualToDiff}}}(\mathbf{r}^k, \mathbf{z}^k)). \quad (15)$$

396 For brevity, we neglect the superscript  $k$  in the following derivation of the proce-  
 397 ssor unit. For each residual layer within the processor unit, we first calculate the resid-  
 398 ual term  $\mathbf{r}$  as follows:

$$\mathbf{r}^t = \mathbf{z}_{acc}^t - \mathbf{z}_{acc}^{t-1} + \mathbf{z}_{adv}^t + \mathbf{z}_{src}^t. \quad (16)$$

399 The above equation is similar to Eq. (3), with the distinction that each term in Eq.  
 400 (3) corresponds to a specific phase. The latent variables in the above equation encom-  
 401 pass representations for both phases. In the first residual layer of each processor block,  
 402 the terms  $\mathbf{z}_{acc}^t$  and  $\mathbf{z}_{acc}^{t-1}$  in Eq. 16 are identical. In other words, the accumulation term  
 403  $\mathbf{z}_{acc}^{t-1}$  sent from the previous processor will serve as both the previous state  $\mathbf{z}_{acc}^{t-1}$  and the  
 404 current state  $\mathbf{z}_{acc}^t$ . Consequently, the previous state  $\mathbf{z}_{acc}^{t-1}$  remains fixed, while the cur-  
 405 rent state  $\mathbf{z}_{acc}^t$  is updated in subsequent residual layers.

406 After calculating the latent residual  $\mathbf{r}^t$ , each of the latent variables (i.e.,  $\mathbf{z}_{acc}^t$ ,  $\mathbf{z}_{adv}^t$   
 407 and  $\mathbf{z}_{src}^t$ ) is multiplied by  $\mathbf{r}^t$ , and their products are sent to the operator  $\mathcal{F}_{\theta_{\text{ResidualToDiff}}}$   
 408 as inputs, expressed as follows:

$$\mathbf{r}_z^t = \mathcal{F}_{\theta_{\text{ResidualToDiff}}} \left( \begin{bmatrix} \mathbf{z}_{acc}^t \\ \mathbf{z}_{adv}^t \\ \mathbf{z}_{src}^t \end{bmatrix} \circ \begin{bmatrix} \mathbf{r}^t \\ \mathbf{r}^t \\ \mathbf{r}^t \end{bmatrix} \right). \quad (17)$$

409 In this step, the output  $\mathbf{r}_z^t$  refers to the term  $-\left(\mathbf{J}^k\right)^{-1} \mathbf{r}^k$  in the latent space. Then,  
 410 the latent residual term  $\delta \mathbf{z}^t$  can be derived as follows:

$$\mathbf{d}_z^t = \mathcal{F}_{\theta_{\text{LatentToDiff}}}(\mathbf{z}^t), \quad (18)$$

$$\delta \mathbf{z}^t = \mathcal{F}_{\theta_{\text{DiffToDiff}}}(\mathbf{d}_z^t \circ \mathbf{r}_z^t), \quad (19)$$

412 where the operator  $\mathcal{F}_{\theta_{\text{LatentToDiff}}}$  is to transform the latent variable into a new term to  
 413 introduce nonlinearity. Then, the operator  $\mathcal{F}_{\theta_{\text{DiffToDiff}}}$  takes the product  $\mathbf{d}_z^t \circ \mathbf{r}_z^t$  as in-  
 414 put and returns the latent residual term  $\delta \mathbf{z}^t$ . Therefore, in each residual layer, the la-  
 415 tent variable  $\mathbf{z}^t$  is updated as

$$\mathbf{z}^t = \mathbf{z}^t + \delta \mathbf{z}^t. \quad (20)$$

416 In this study, the design of the residual layer is heuristic, as the updating proce-  
 417 dure is performed in a high-dimensional latent space and is parameterized by neural net-  
 418 works. The high-dimensional representation enables the latent variable to capture com-  
 419 prehensive information about the input variables. The processor unit in this study is re-  
 420 ferred to as a residual-based processor, as it is composed of residual layers and draws in-  
 421 spiration from the concept of residuals in the governing equations.

### 422 3 Experimental Setup

423 In this study, we conduct a comprehensive evaluation of the proposed physics-encoded  
 424 DL model through three distinct experiments. First, we assess the predictive capabil-  
 425 ity of the model using unseen permeability inputs in Section 4.1 and compare our model  
 426 with the Recurrent R-U-Net over the public dataset proposed by M. Tang et al. (2021).  
 427 Second, we investigate the model's performance in the presence of unseen pairs of con-  
 428 trol variables and permeability inputs (Section 4.2). This assessment requires the model  
 429 to generalize and handle complex and diverse scenarios. Lastly, we explore the model's

430 extrapolation capability by applying it to the prediction over the post-injection period  
 431 while the training set only covers the injection period (Section 4.3). This extrapolation  
 432 task poses a significant challenge due to the distinctive dynamics involved. In addition  
 433 to these three experiments, we investigate the effect of the physics-based encoder on the  
 434 latent representations of the governing terms by replacing the physics-based encoder with  
 435 a traditional convolutional encoder (Section 4.4).

436 In addition to the comparison based on publicly available datasets (M. Tang et al.,  
 437 2021), we also applied our model to a set of simulated datasets generated by a synthetic  
 438 3D simulation model of deep saline aquifer (Appendix C). The training datasets include  
 439 simulation models for both single-well and two-well scenarios, introducing sufficient di-  
 440 versity in the dataset. However, we test our model on the two-well scenario only, as it  
 441 is more complex than the one-well scenario. The simulation model consists of CO<sub>2</sub>  
 442 injection over 15 years, followed by a post-injection period of 85 years. For our third ex-  
 443 periment, we specifically utilize the initial 15 years of the post-injection as our test set.  
 444 This selection is based on the observation that the pressure and plume dynamics reach  
 445 a quasi-steady state beyond this time frame and do not show observable changes over  
 446 time. The simulated dataset consists of 30 steps, where each step represents one year.  
 447 During the injection, the well controls are randomly perturbed for each year while be-  
 448 ing constrained to have a total injection amount over 15 years. For detailed information  
 449 regarding the simulation model and data generation, please refer to Appendix C.

450 In the examples with the public dataset, the models are trained to predict the whole  
 451 simulation time with 10 steps by taking the initial state and permeability as inputs, fol-  
 452 lowing the setup in M. Tang et al. (2021). In the other experiments conducted in this  
 453 study, however, the training process involves feeding the models with dynamic states from  
 454 any time step and predicting only the subsequent 8 years rather than the entire 15 years.  
 455 Exposing the model to dynamic inputs of different time frames can enable models to pre-  
 456 vent overfitting and accurately learn the dynamics. Consequently, each training sample,  
 457 comprising 16 time frames (15 years plus an initial state), is divided into eight data sam-  
 458 ples, each spanning 8 time frames. During testing, the DL models predict the entire 15  
 459 years over injection (or 30 years over both injection and post-injection periods) without  
 460 taking any ground truth dynamic state as input.

461 In the experiment on the public dataset, we propose a modified version of Recur-  
 462 rent R-U-Net by making three key modifications to the architecture of the original model  
 463 proposed by M. Tang et al. (2021). These modifications were aimed at improving the  
 464 model's performance and aligning it with the setup of our model to ensure fair and mean-  
 465 ingful comparisons. First, we replaced Batch Normalization (BatchNorm) (Ioffe & Szegedy,  
 466 2015) in the original model with Group Normalization (GroupNorm) (Y. Wu & He, 2018).  
 467 This change was motivated by the observation that GroupNorm offers better general-  
 468 ization and transferability compared to BatchNorm (Kolesnikov et al., 2020). Second,  
 469 we introduced a dummy control input to the modified Recurrent R-U-Net and our model  
 470 for the public dataset. The control variable in the public dataset is fixed over time and  
 471 not included as input in the original Recurrent R-U-Net. This change is to make the use  
 472 of modified Recurrent R-U-Net and our model consistent throughout this work. The dummy  
 473 control variable for each time step is a 3D tensor, with values of 0 for grid blocks with  
 474 no well, 1 for producers, and -1 for injectors. Lastly, we redefined the static variable  $\mathbf{m}$   
 475 by 1) adding  $\mathbf{I}_{PV}$  and  $\mathbf{D}$  as part of the input, and 2) replacing permeability  $\mathbf{K}$  with the  
 476 term  $\mathbf{T}_m$ .

477 The pressure and injection rate are normalized using Min-Max normalization. Sat-  
 478 uration is not normalized since it typically ranges between 0 and 1. To normalize the in-  
 479 verse grid volume  $\mathbf{I}_{PV}$ , we scale it by multiplying a reference grid volume of 50×50×  
 480 2.5 m<sup>3</sup>. Using a uniform layer thickness, the depth  $\mathbf{D}$  varies from 0 to 19, representing  
 481 the depths of grid blocks from the first to the 20th layer. The term  $\mathbf{T}_m$  contains zero  
 482 values to represent the closed boundary and exhibits a right-skewed distribution with

483 a mean significantly higher than the median. Consequently, we apply the inverse hyper-  
484 bolic sine transformation to transform  $\mathbf{T}_m$  before feeding it into a deep learning model.

485 The training in this study employs the Adam optimizer. In our proposed model  
486 and the modified Recurrent R-U-Net, we apply the relative  $\ell_2$ -loss (Wen et al., 2022) as  
487 the loss function, which is defined as follows:

$$L(\{\mathbf{S}, \mathbf{p}\}_{t_1:t_2}, \{\hat{\mathbf{S}}, \hat{\mathbf{p}}\}_{t_1:t_2}) = \frac{\|\mathbf{S}_{t_1:t_2} - \hat{\mathbf{S}}_{t_1:t_2}\|_2}{\|\mathbf{S}_{t_1:t_2}\|_2} + \frac{\|\mathbf{p}_{t_1:t_2} - \hat{\mathbf{p}}_{t_1:t_2}\|_2}{\|\mathbf{p}_{t_1:t_2}\|_2}, \quad (21)$$

488 where  $\{\hat{\mathbf{S}}, \hat{\mathbf{p}}\}_{t_1:t_2}$  represents the predicted saturation and pressure over time steps from  
489  $t_1$  to  $t_2$ . In this work, the variance of the norms  $\|\mathbf{S}_{t_1:t_2}\|_2$  or  $\|\mathbf{p}_{t_1:t_2}\|_2$  are considerably  
490 high due to the dynamic range of time frames, which can vary widely. Using the mean  
491 squared error (MSE) loss function encourages inaccurate predictions at the start of in-  
492 jection. This is mainly because the saturation of the non-wetting phase in the initial time  
493 frames is inconsequential. Deep learning models that fail to predict the saturation of these  
494 time frames will still generate low values of MSE loss. The choice of relative error as the  
495 loss function will mitigate this issue. The details of the training process and configura-  
496 tion are provided in Appendix B.

## 497 4 Results and Discussion

### 498 4.1 Testing on Unseen Permeability

499 In this experiment, we first compare three models on the public dataset (M. Tang  
500 et al., 2021): the original Recurrent R-U-Net (the baseline model), the modified Recur-  
501 rent R-U-Net, and our proposed model. The dataset consists of 2923 samples spanning  
502 1000 days and is generated by a numerical simulation model of a two-phase oil reservoir  
503 for a waterflooding problem. In this experiment, models are trained to predict oil sat-  
504 uration using different amounts of training samples: 200, 500, 1000, 1500, 2000, and 2500.  
505 A separate set of 50 samples is used for model validation, while the remaining 373 sam-  
506 ples form the test set.

507 Figure 4 (a) shows that our model consistently achieves lower test losses across all  
508 sizes of training samples compared to the other two models. Notably, our model trained  
509 on 1000 samples demonstrates a comparable root mean square error (RMSE) of satu-  
510 ration prediction to the baseline model trained on 2500 samples. Figure 4 (b) demon-  
511 strates the distribution of saturation RMSE for each time step, where the baseline model  
512 exhibits higher mean and variance in test losses across time steps compared to our model.  
513 To further evaluate the saturation predictions, Figure 5 visualizes the 3D saturation pre-  
514 diction at the 10th time step. The baseline model trained with 200 samples shows a sig-  
515 nificant mismatch in the saturation front. Both modified Recurrent R-U-Net and our model  
516 accurately capture the saturation front for both the 200 and 2500 training sample cases  
517 with lower RMSE values. In the subsequent experiments, we will continue using the mod-  
518 ified Recurrent R-U-Net for comparison and exclude the original version. The original  
519 Recurrent R-U-Net has a different setup of input and does not support time-varying con-  
520 trol variables.

521 Next, we proceed to evaluate our model in the simulation model of subsurface CO<sub>2</sub>  
522 storage reservoir. Our proposed model and modified Recurrent R-U-Net are trained us-  
523 ing 700 simulated samples to predict pressure and CO<sub>2</sub> saturation over a 15-year injec-  
524 tion. The 700 simulated samples are then divided into 5600 training data samples, each  
525 of which spans eight years. The validation and test sets consist of 100 and 200 simulated  
526 samples, respectively. The training and test sets have the same injection controls but dif-  
527 ferent permeability. For brevity, we will refer to the modified Recurrent R-U-Net as RUNET  
528 in the following experiments. As shown in Figure 6, our proposed model consistently ex-  
529 hibits lower mean and variance of RMSE compared to RUNET. It is worth noting that

530 the saturation error exhibits increasing trends over time due to the spreading of the sat-  
 531 uration front. In contrast, the pressure error is more stationary, attributed to the pres-  
 532 ence of an aquifer region surrounding the storage reservoir, which facilitates pressure dis-  
 533 sipation and maintains it within a certain range.

534 Figures 7 and 8 provide 3D visualizations of saturation and pressure distributions,  
 535 respectively. The errors in both saturation and pressure tend to occur in areas where there  
 536 are significant changes (or gradients). Specifically, for saturation, the errors are promi-  
 537 nent near the front of the CO<sub>2</sub> plume, where the saturation values experience rapid transi-  
 538 tions. On the other hand, for pressure, the errors are more noticeable in the vicinity  
 539 of the wells. The 3D pressure map changes significantly over time due to variations in  
 540 injection control. As reflected in Figures 7 and 8, our model outperforms the RUNET  
 541 in capturing these two distinct patterns.

#### 542 4.2 Testing on Unseen Control and Permeability

543 In this experiment, we further evaluate the performances of two models (our model  
 544 and RUNET) on the test set where both control and permeability are unseen during train-  
 545 ing. The training, validation, and test sets still consist of 700, 100, and 200 simulated  
 546 samples, respectively. As depicted in Figure 9, the distribution of injection rates differs  
 547 between the training and test sets, even though both datasets have the same constraint  
 548 of total injection rate. Notably, the allocation of injection rates in the test set exhibits  
 549 more significant variations compared to the training set, demonstrating a less balanced  
 550 allocation of injection rates. The allocation of the injection rate for the test set falls out-  
 551 side the distribution covered by the training set. For control optimization problems, the  
 552 control variable can evolve towards its extremity during the process of optimization (Qin  
 553 et al., 2023). The out-of-distribution injection rate resembles the challenges caused by  
 554 the extremity of the control variable in the optimization task and challenges the model's  
 555 robustness in handling diverse control scenarios (Qin et al., 2024).

556 Figure 10 illustrates that the prediction performances of the two models are com-  
 557 parable in predicting pore pressure, while our model is more accurate in predicting sat-  
 558 uration than RUNET. Given the variations in control variables in the test set, predict-  
 559 ing saturation and pressure becomes more challenging for both models compared to the  
 560 previous experiment. Figures 11 and 12 provide visualizations of saturation and pore pres-  
 561 sure predictions for both models. In Figure 11, it can be observed that the saturation  
 562 prediction from RUNET shows significant errors around the top layer, leading to phys-  
 563 ically inconsistent results. In contrast, our model exhibits only slight discrepancies near  
 564 the saturation front in the top layer, indicating its improved accuracy and ability to main-  
 565 tain consistency with the underlying physics. As shown in Figure 12, the pressure pre-  
 566 diction from RUNET exhibits errors that are evenly distributed around the wells, while  
 567 the prediction error from our model is more concentrated. This distinct behavior between  
 568 the two models may be attributed to differences in their architectures and will be fur-  
 569 ther investigated in our future work.

#### 570 4.3 Extrapolation over Post-Injection

571 In the previous experiments, the deep learning models were trained and tested over  
 572 a 15-year injection. During testing, DL models predicted the future states over the same  
 573 period based on different sets of inputs. In this experiment, we extend the application  
 574 of these trained models to predict 30 years, including both injection and post-injection.  
 575 Specifically, models trained in previous experiments (Sections 4.1 and 4.2) are directly  
 576 applied to predict the last 15 years, from the 16th to the 30th year, with the initial state  
 577 to be predicted saturation and pressure in the 15th year. During post-injection, injec-  
 578 tion rates are set to zero.

579 In Figure 13, the prediction performances of two models are evaluated for both in-  
 580 jection and post-injection periods. It can be observed that our model consistently ex-  
 581 hibits significantly lower prediction errors for saturation than RUNET. Furthermore, our  
 582 model's prediction errors remain relatively stable during post-injection, whereas errors  
 583 from RUNET keep increasing for the saturation prediction. On the other hand, the pore  
 584 pressure of the entire reservoir becomes more uniform and converges to the boundary  
 585 pressure during post-injection. Therefore, pressure prediction becomes less challenging  
 586 for the two models, as both exhibit decreasing prediction errors after the 15th year when  
 587 the post-injection starts. Despite the comparable performance of pressure prediction for  
 588 both models during the injection period (Figure 13 (d)), our model consistently outper-  
 589 forms RUNET in terms of lower mean and variance of prediction errors during post-injection.  
 590 This indicates the superior robustness and accuracy of our model in handling the dis-  
 591 tinct dynamics of the post-injection period.

592 Figure 14 visualizes three examples of the saturation predictions for two models  
 593 in the 15th and 30th years. It can be observed from all three examples that, during the  
 594 post-injection period, CO<sub>2</sub> is dominantly driven by the buoyant force and gets accumu-  
 595 lated at the top layer, which is overburdened by cap rock. A common failure of RUNET  
 596 is its physically inconsistent prediction during extrapolation. As shown in the first two  
 597 examples, the predicted CO<sub>2</sub> plume from RUNET in the 30th year shows disconnected  
 598 patterns and deviates significantly from the ground truth. In the last two examples, the  
 599 prediction from RUNET exhibits a relatively low RMSE in the 15th year, which is close  
 600 to the error of our model. However, RUNET still fails to capture the CO<sub>2</sub> migration dur-  
 601 ing post-injection and even shrinks the CO<sub>2</sub> plume toward the end of the prediction. On  
 602 the other hand, our model can accurately extrapolate the CO<sub>2</sub> plume during extrap-  
 603 olation. Over three models, our model accurately predicts the saturation front compared  
 604 with a slight increase in RMSE.

605 Figure 15 visualizes the pressure prediction of the 17th layer of the reservoir for  
 606 two models during post-injection. It can be observed that the pressure dissipates dur-  
 607 ing post-injection and reaches the aquifer boundary, which serves as a constant bound-  
 608 ary condition due to its extensive volume. In contrast to RUNET, our model demon-  
 609 strates an accurate prediction of the pressure dissipation and eventual convergence to the aquifer  
 610 pressure. These findings underscore the superior performance of our model in captur-  
 611 ing long-term behavior and accurately predicting the saturation evolution beyond the  
 612 injection period.

613 It is important to note that predicting the post-injection period is an extrapola-  
 614 tion task, as it falls outside the time range covered by the training set. Extrapolation  
 615 tasks can pose challenges for deep learning models, as the statistical input-output rela-  
 616 tionship during extrapolation may deviate from what was learned from the training set.  
 617 In the case of CO<sub>2</sub> migration, the dominant driving force changes between the injection  
 618 and post-injection periods, which can result in a different statistical input-output rela-  
 619 tionship. This change in driving force can undermine the prediction performance of deep  
 620 learning models. Therefore, accurate prediction during post-injection requires the mod-  
 621 els to capture the underlying physics of the system, rather than solely relying on the learned  
 622 statistical relationship from the training set.

#### 623 4.4 Investigation of Latent Representation

624 To further investigate the effect of introducing the physics-based encoder on the  
 625 prediction performance, we introduce an additional DL model. This model shares the  
 626 identical modules as the proposed physics-encoded DL model, with the exception that  
 627 the physics-based encoder is replaced with convolutional encoders. This alteration fa-  
 628 cilitates a more focused investigation of the effect. The convolutional encoder comprises  
 629 two separate encoders to produce the latent representations of accumulation and advec-

630 tion terms, respectively. Each encoder shares a similar architecture as the encoder in the  
 631 RUNET. In the case of the accumulation term, the input exclusively encompasses the  
 632 initial states of dynamic variables (i.e., pressure and saturation). As for the advection  
 633 term, dynamic and static variables are concatenated together and fed into the encoder  
 634 as input. Subsequently, the latent variables representing the accumulation and advect-  
 635 ion terms are then sent to the processor blocks, the same as the pathway of the physics-  
 636 based encoder.

637 Figure 16 illustrates the comparison between two models: one equipped with the  
 638 physics-based encoder (referred to as "Ours") and the other with convolutional encoders  
 639 (referred to as "ConvEnc"). Both models are trained and tested using the same setup  
 640 as the second experiment (Sec. 4.2). The results show that both models demonstrate sim-  
 641 ilar RMSE values for pressure and saturation during injection. However, our model con-  
 642 sistently outperforms ConvEnc during the post-injection period. On the other hand, as  
 643 shown in Figure 17, ConvEnc significantly outperforms RUNET in predicting pressure  
 644 and saturation, encompassing both injection and post-injection periods. Given that all  
 645 three models possess a similar number of trainable parameters (over 3 million), these re-  
 646 sults exhibit the superior performances of the physics-based encoder and the residual-  
 647 based processor in contrast to the convolutional encoder and ConvLSTM, respectively.

648 Since the governing terms follow certain PDE constraints, it is essential to construct  
 649 a compact latent space. The latent representations of accumulation and advection terms  
 650 are expected to exhibit similar patterns with the true governing terms to contain phys-  
 651 ically consistent features. Therefore, we further investigate the latent representations of  
 652 two governing terms derived from our model and ConvEnc and discuss their physical mean-  
 653 ings. Figure 18 illustrates an example of the latent representations of accumulation (Fig-  
 654 ure 18 (a)) and advection terms (Figure 18 (b)) over the first 15 years for both our model  
 655 and ConvEnc. The collected latent representations are the outputs of the last proces-  
 656 sor layer. To reduce the redundancy in latent representations, we first employ Princi-  
 657 pal Component Analysis (PCA) on  $d_l$  latent variables ( $d_l = 32$ ) for each time step sep-  
 658 arately. Here, only the first four principal components (PCs) are visualized in Figure 18  
 659 for brevity. Moreover, Figures 18 (a) and 18 (b) present the actual values of the wetting-  
 660 phase accumulation and advection in the vertical direction in the 13th year as references.

661 As shown in Figure 18 (a), the true accumulation term is dominantly affected by  
 662 saturation (Figure 18 (d)), with only slight variations outside the CO<sub>2</sub> plume as affected  
 663 by pressure (Figure 18 (c)). This slight variation is because the density of liquid-phase  
 664 water is insensitive to pressure changes and that reservoir porosity is set to be homo-  
 665 geneous in this work. The components from our model exhibit similar patterns with pres-  
 666 sure contour and saturation front, as reflected in the first and third components. The  
 667 components from ConvEnc also reflect these two features, as shown in the first PC. How-  
 668 ever, as depicted in the second PCs, the latent accumulation terms in ConvEnc exhibit  
 669 high-frequency patterns similar to permeability. This arises from the updating process  
 670 within the processor blocks, where the latent accumulation and advection mutually in-  
 671 fluence each other. These high-frequency patterns are distinct from the accumulation  
 672 terms depicted in Figure 18 (a). The residual-based processor model passes the latent  
 673 accumulation to the next time step to approximate the dynamics of the mass balance  
 674 governing equation. Latent representations that are not aligned with the true govern-  
 675 ing terms could hinder the learning process and lead to inefficient learning of the dynam-  
 676 ics.

677 Figure 18 (b) illustrates the PCs of latent representations of the advection term  
 678 for both models. Notably, the latent advection terms generated by our model closely align  
 679 with the true values and exhibit high-fidelity patterns. In contrast, ConvEnc produces  
 680 overly smoothed latent advection patterns. This distinction between the two models may  
 681 stem from the inclusion of the physics-based encoder. Specifically, in our model, the over-  
 682 all receptive field for permeability spans only three grid blocks. This design choice pre-

vents over-smoothness during the calculation of the latent advection term, thus preserving intricate details. On the other hand, ConvEnc's receptive field follows the default setup of RUNET and spans 12 blocks, resulting in an inconsistent inductive bias with the advection term. While ConvEnc can learn high-fidelity patterns from the data, it requires more data to constrain its behavior, hindering efficient learning. Furthermore, components within ConvEnc's latent advection term exhibit temporal inconsistency, with notable shifts in patterns observed in the third PCs. This behavior presumably correlates with the unexpected updating caused by physically inconsistent latent variables. Despite our model's superiority over ConvEnc, we do not dive into introducing any metrics to evaluate the physical consistency of latent variables. This aspect extends beyond the scope of this work and could potentially be explored in future endeavors.

## 5 Conclusion

In this work, we propose novel DL architectures that incorporate the physics of the system for accurate spatial-temporal prediction of pressure and saturation in geologic CO<sub>2</sub> storage. Traditional deep learning models, which solely rely on learning statistical input-output relationships, face challenges in extrapolation, require large amounts of training data, and can produce physically inconsistent predictions. Additionally, these models struggle to adapt to general input-output setups involving diverse types of inputs and outputs. To address these limitations, we introduce a general approach that efficiently learns the underlying physics by encoding physics into the encoder and processor. We demonstrate the ability to learn the underlying physics, handle permeability variations and time-varying controls, and make predictions over both the injection and post-injection periods. As one of the main contributions, the physics-based encoder generates physically meaningful latent variables through physical operators and high-dimensional projection. The physical operators constrain the dependencies of latent variables on inputs and reduce the search space for the model's parameter. The operators within the residual-based processor update the high-dimensional latent variables in a coupled manner. The updating process within high-dimensional latent space enables the integration of non-linear and coupled PDEs, bypassing the need for assumption and simplification that are necessary for direct updating pressure and saturation.

The experimental results validate the effectiveness of our proposed model in addressing the aforementioned limitations faced by traditional deep learning models. Our model exhibits data efficiency, as demonstrated on a public dataset (Section 4.1), and consistently outperforms traditional deep learning models when handling various types of inputs (Sections 4.1 and 4.2). The physical operators enable our model to approximate the underlying physics and learn the complex input-output relationship efficiently. Furthermore, our model exhibits superior performance compared to RUNET in the extrapolation to the post-injection period (Section 4.3), where RUNET fails to extrapolate the saturation front and generates physically inconsistent predictions. The recurrent architecture, along with regular time intervals for each recurrent unit, allows our model and RUNET to effectively predict over arbitrary lengths of time steps. However, in contrast to RUNET which lacks interpretability and remains a black box, our model comprises modular components that serve specific roles in the evolution of dynamics.

The generalizability and applicability of our model extend beyond geologic CO<sub>2</sub> storage and the specific scenarios studied in this work. Notably, the public dataset used in Section 4.1 focuses on a waterflooding problem with producers and injectors controlled by BHP. Therefore, the proposed architecture is not limited to geologic CO<sub>2</sub> storage or a specific type of well control. Instead, it can be adapted and applied to other geoscience and engineering domains where accurate spatial-temporal predictions are crucial, such as waterflooding and geothermal applications. The model's generalizability of handling different reservoir settings and time-varying controls makes it a valuable tool for decision-making and inverse modeling across a wide range of applications. Moreover, the gener-

735 alizability of the DL model could potentially address the challenge of limited available  
736 datasets in scientific domains, where data acquisition is often expensive and relatively  
737 scarce compared to domains like computer vision and natural language processing. The  
738 available datasets online typically differ in input setups, and traditional deep learning  
739 models are only applicable to a certain instance. Deep learning models with flexible and  
740 general-purpose architectures, such as ours, can make efficient use of the available data  
741 and alleviate the limitations imposed by data scarcity. This is particularly crucial for the  
742 development and practical application of powerful yet typically large deep learning mod-  
743 els in real-world scenarios.

744 Although our model primarily focuses on variations in control and permeability,  
745 this work provides a general and flexible approach that can be extended to various in-  
746 puts in future studies (e.g., heterogeneous porosity, different well locations, and differ-  
747 ent reservoir sizes). Another promising future work is to integrate physics-informed loss  
748 functions into our model to enable data-free training or zero-shot learning. PINN demon-  
749 strates proficiency in learning simpler tasks but faces limitations with complex tasks (Krishnapriyan  
750 et al., 2021). For the geologic CO<sub>2</sub> storage, the nonlinearity and complexity of PDEs could  
751 hinder the training of PINN. One potential solution to address this limitation is to first  
752 pretrain the model with labels and subsequently fine-tune it using a physics-informed  
753 loss function.

## Figures

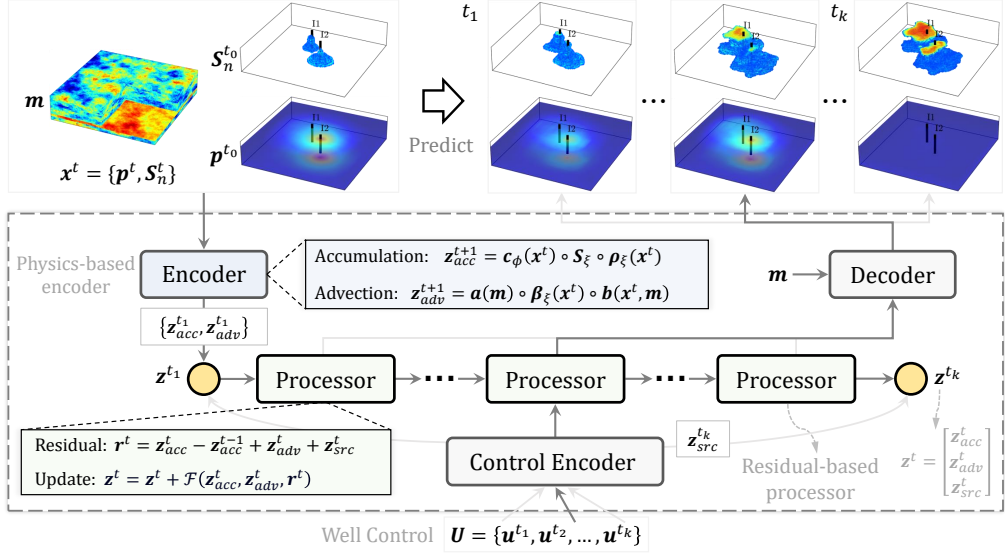


Figure 1: Overview of the proposed Fluid Flow-based Deep Learning (FFDL) model for predicting spatial-temporal pressure and saturation in geologic CO<sub>2</sub> storage. The process is applied to the entire reservoir with four modules: the physics-based encoder and control encoder to project input into physically meaningful latent variables; the residual-based processor to evolve the latent variables given well controls; and the decoder to project latent variables back to pressure and saturation.

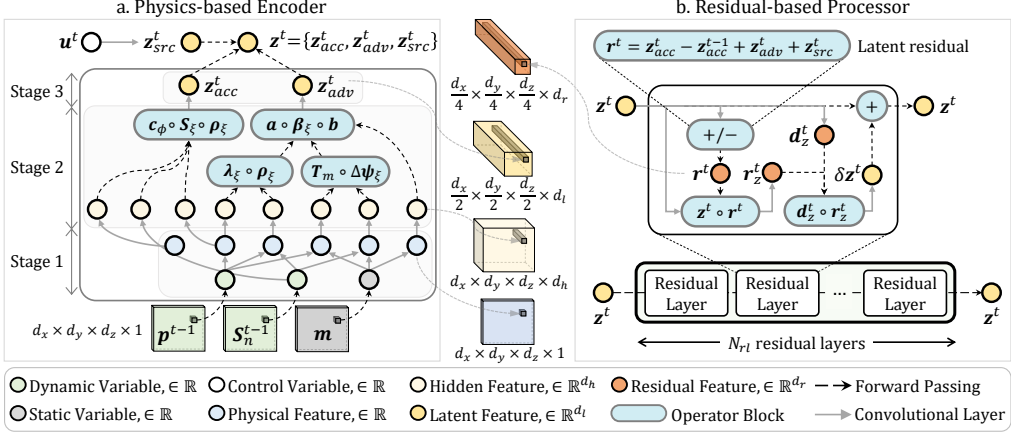


Figure 2: Overview of the physics-based encoder (left) and the residual-based processor (right). Each circle represents a variable corresponding to a single voxel in the 3D representation of the reservoir. The encoder consists of three stages: 1) mapping the inputs (dynamic and static) to physical features, 2) mapping previous features to hidden features, and 3) calculating physical latent variables. For each time step, the processor utilizes a series of residual layers to iteratively update the latent variables. The operator block incorporates non-parametric operators, including Hadamard product, addition, and subtraction. The forward passing operation involves directly passing the variable to the next layer without any additional transformations or modifications.

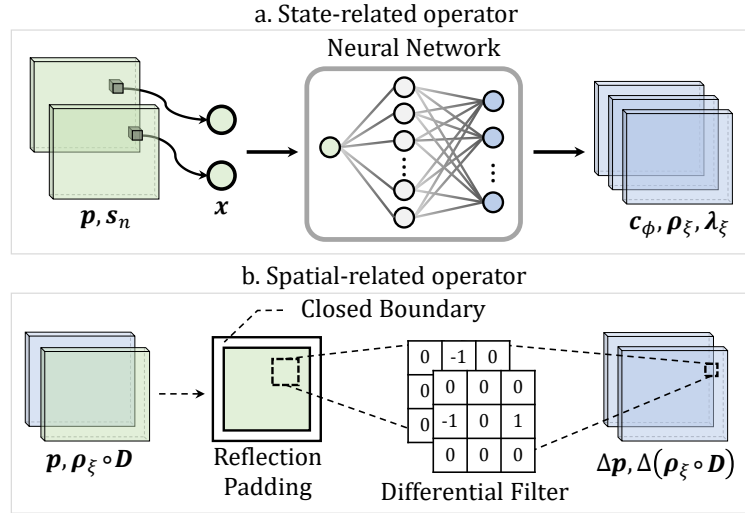


Figure 3: Illustration of (a) state-related operator and (b) spatial-related operator in the first stage of the physics-based encoder. The state-related operator is parameterized by a fully connected neural network. The differential pressure (or fluid potential) is calculated under a closed boundary, which is approximated by reflection padding.

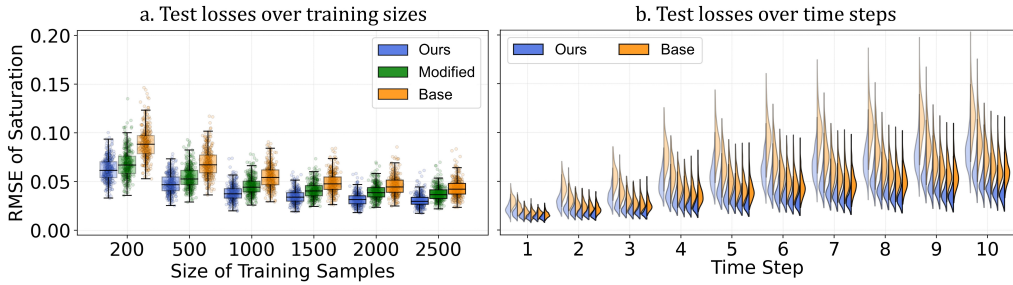


Figure 4: Distributions of test losses of saturation for different models. a. Test losses for different sizes of training samples. b. Test losses of saturation for different time steps. The different transparencies in (a) represent the various sizes of training samples ranging from 200 to 2500 from left to right. Each time step in (b) contains the six bars to represent distributions of RMSE values for the cases of training samples ranging from 200 to 2500 from left to right. "Modified" refers to the modified Recurrent R-U-Net. "Base" refers to the baseline R-U-Net. "Ours" refers to our model.

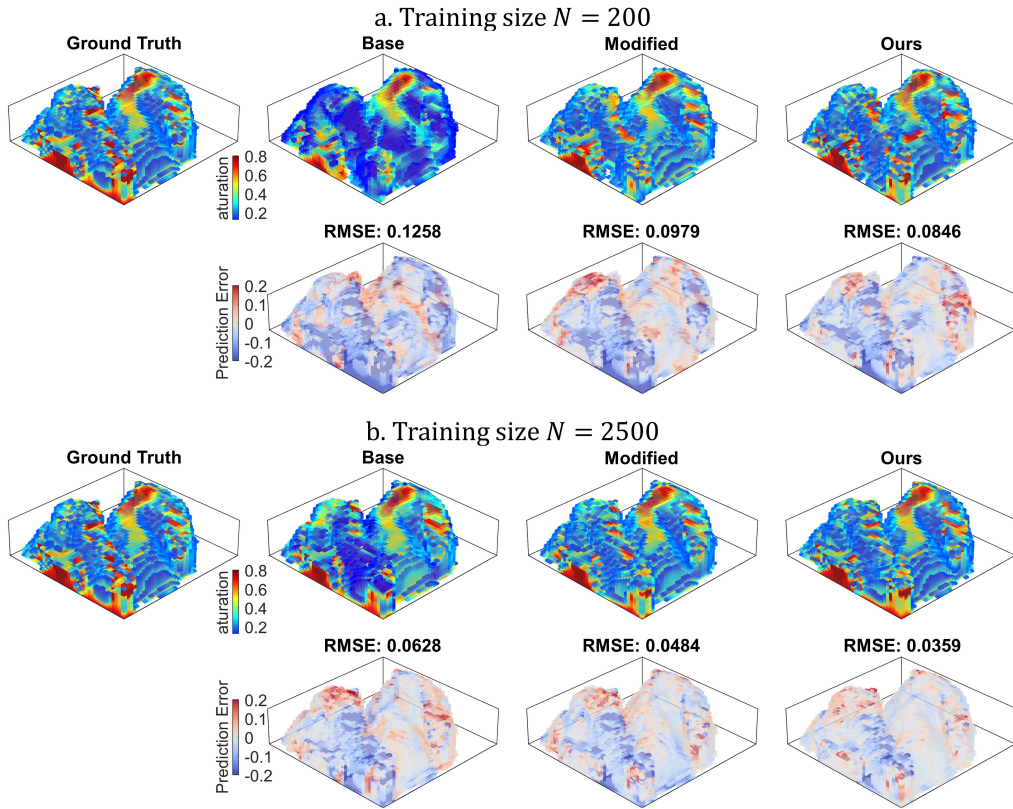


Figure 5: Visualization of predictions of oil saturation exceeding 0.15 at the last time step for three different models trained with varying numbers of training samples: (a) Model trained with 200 samples; (b) Model trained with 2500 samples.

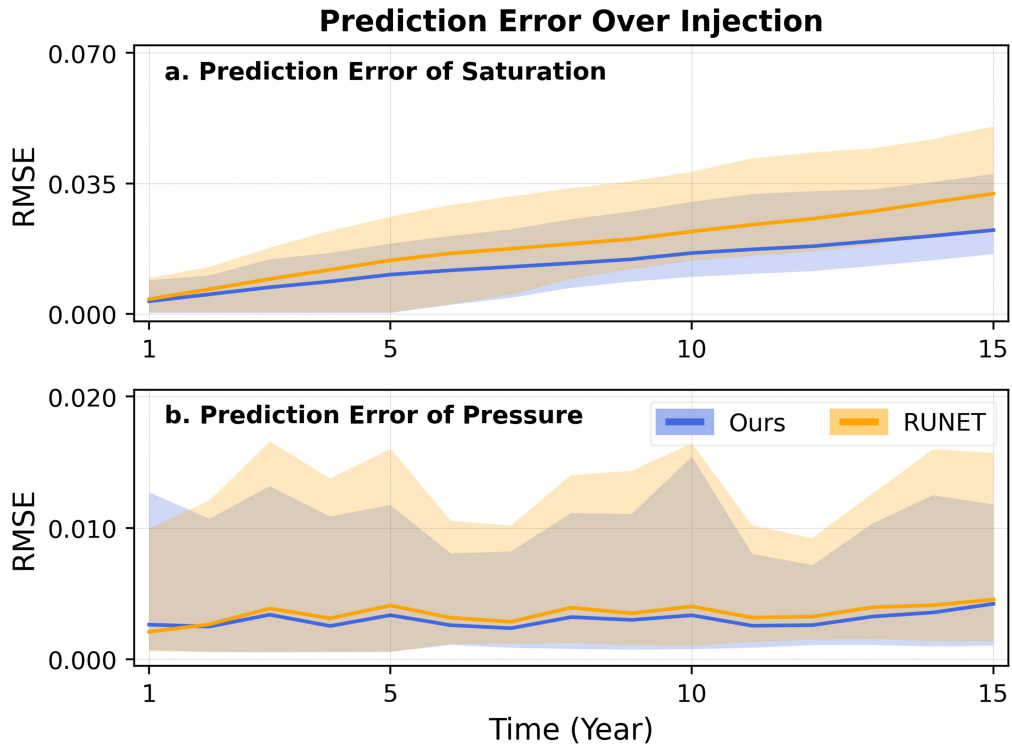


Figure 6: Prediction errors of normalized saturation and normalized pressure over the test set for two models: our proposed model (Ours) and modified Recurrent R-U-Net (RUNET). The error band and solid line represent a 95% confidence interval and the median of RMSE, respectively.

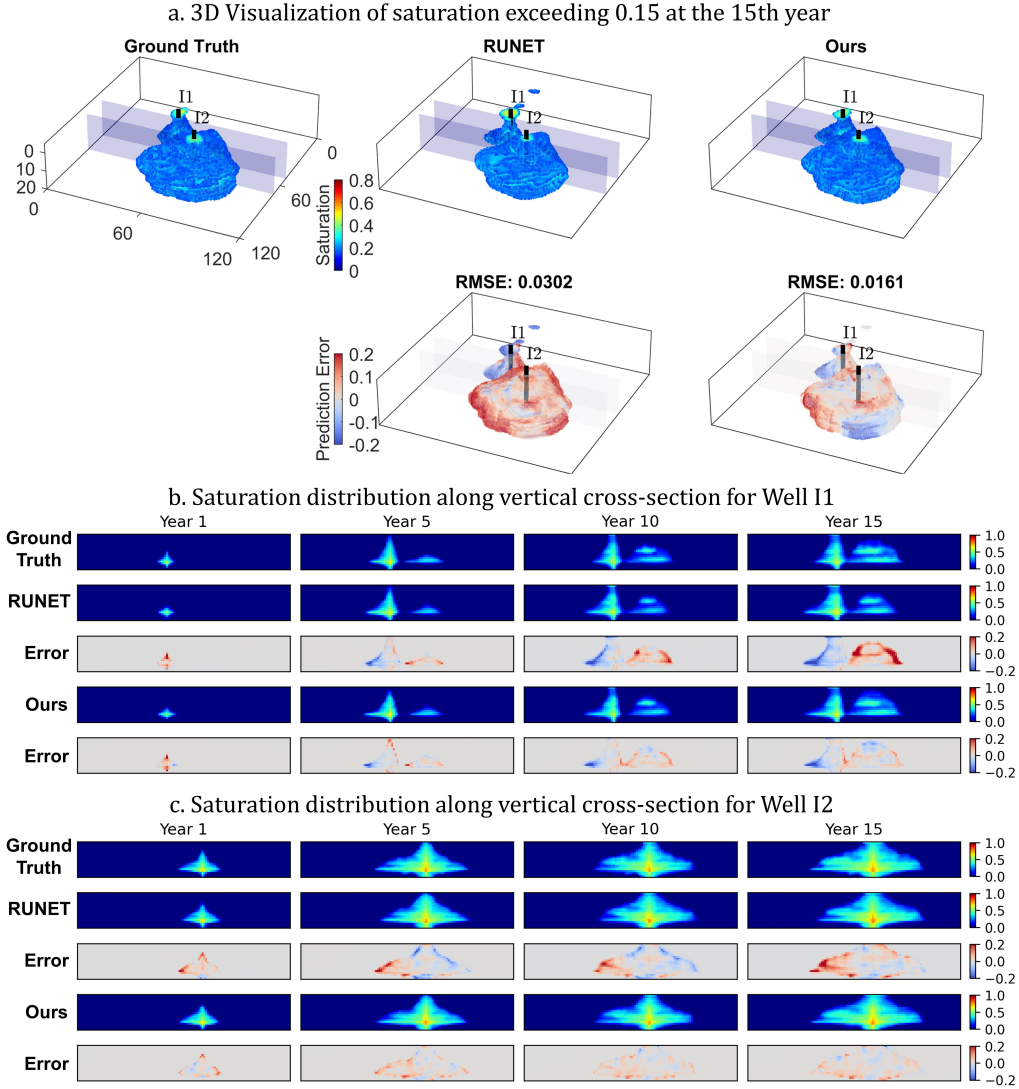


Figure 7: Visualization of saturation prediction over unseen permeability. The 3D visualization in (a) displays the saturation distribution in the 15th year. In (b) and (c), the 2D saturation distributions represent the x-z planes intersecting Wells I1 and I2, respectively. These planes are depicted as transparent cross-sections in (a).

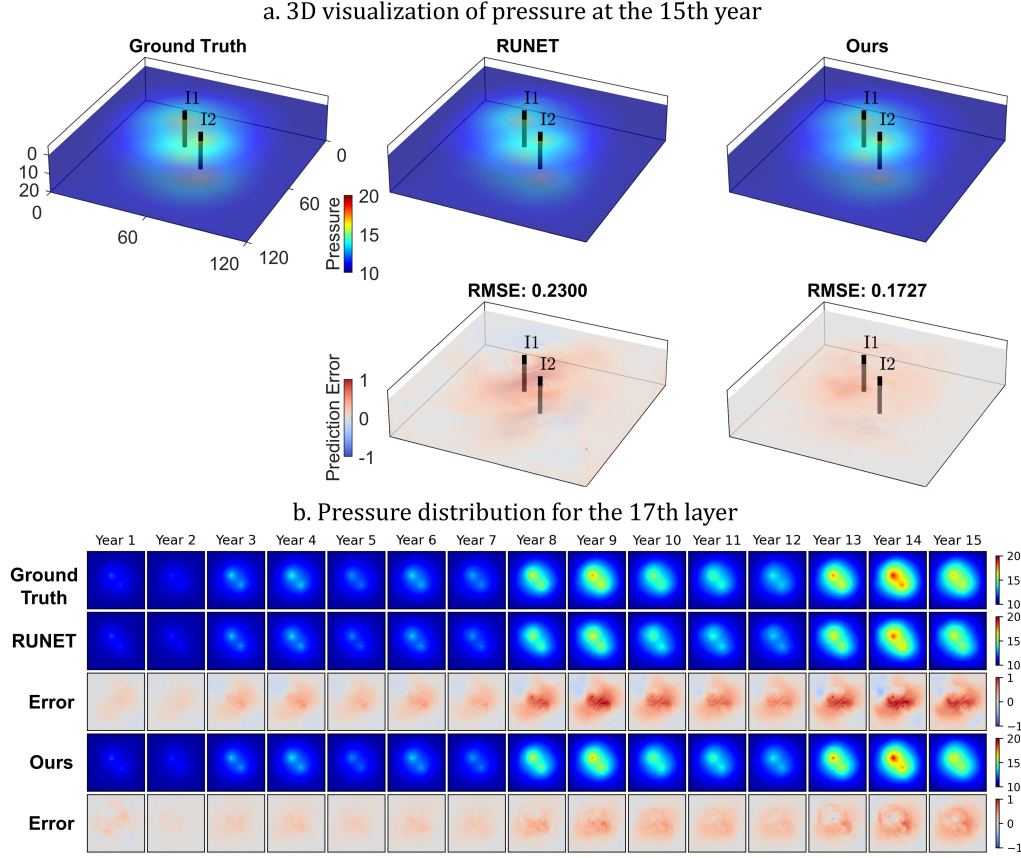


Figure 8: Visualization of pressure prediction over unseen permeability. In (b), the 2D pressure distributions represent the 17th layer of the reservoir, the layer where injection wells are located. The pressure values are measured in MPa, and the RMSE is also reported in MPa.

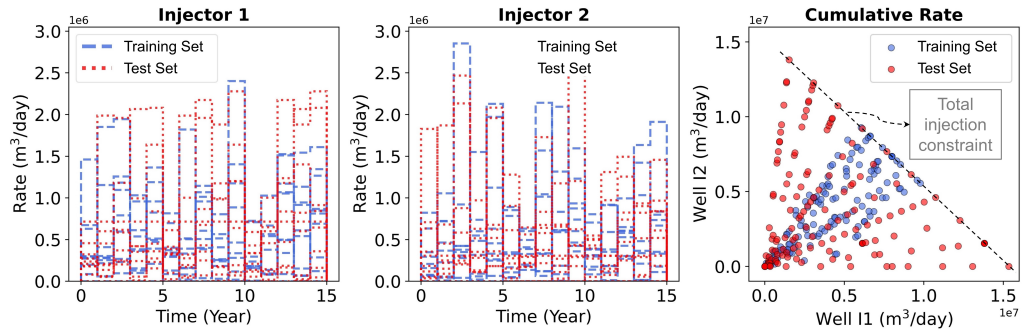


Figure 9: Visualization of injection control in the training and test sets. The left and middle figures depict the time-series injection rates for wells I1 and I2, respectively. The right figure shows the QQ-plot of cumulative injection rates for the two wells, illustrating the differences in the distribution between the two datasets.

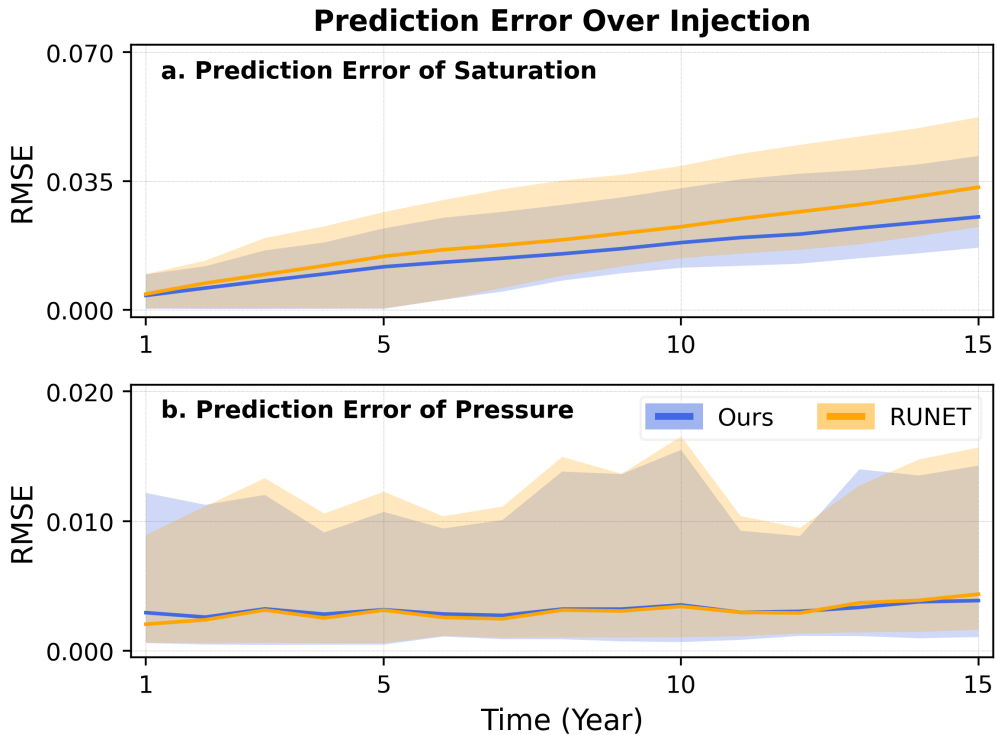


Figure 10: Prediction errors of normalized saturation and pressure over the test set for two models: our proposed model (Ours) and modified Recurrent R-U-Net (RUNET). The error band and solid line represent a 95% confidence interval and the median of RMSE, respectively.

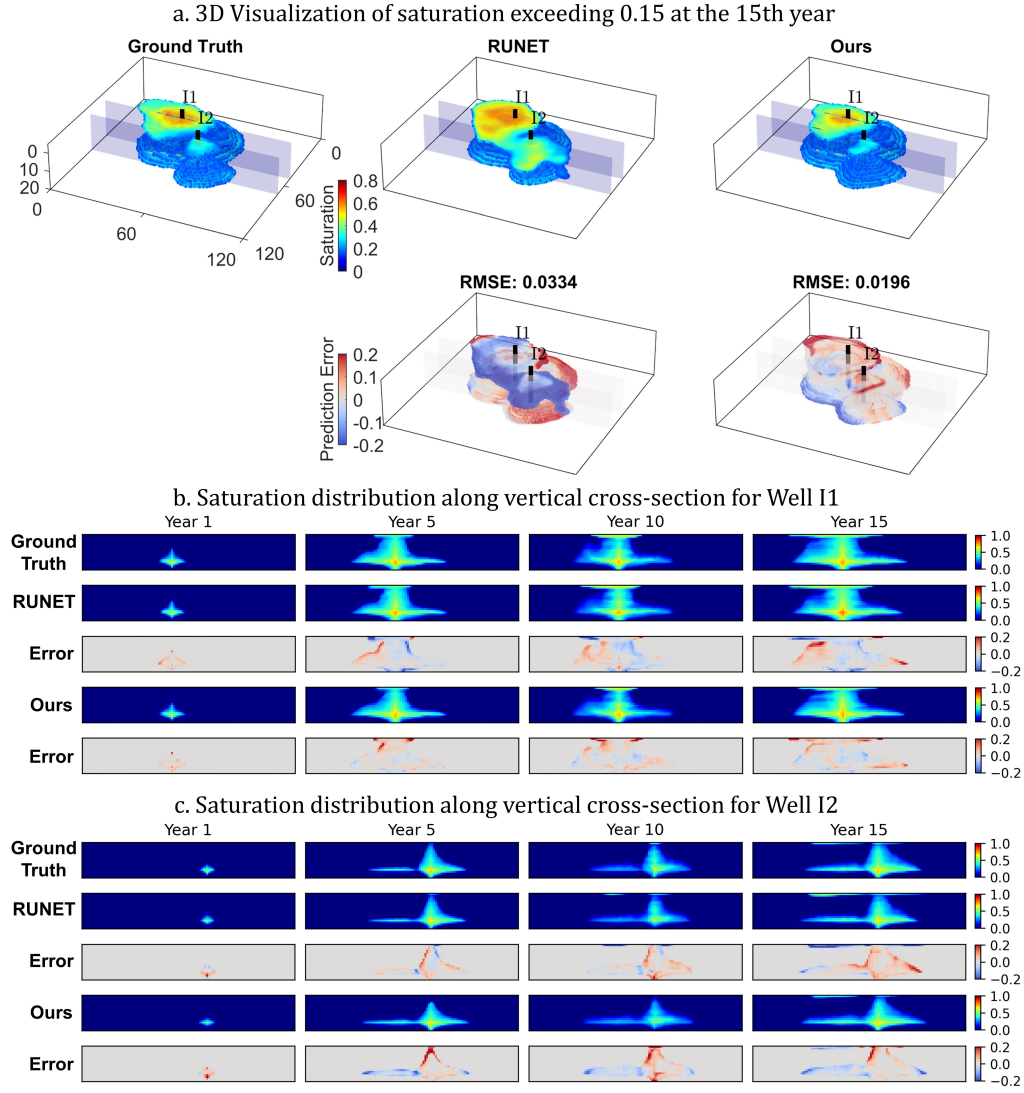


Figure 11: Visualization of saturation prediction over unseen control and permeability. The prediction from RUNET exhibits physical inconsistency and shows a significant mismatch in the shape of saturation.

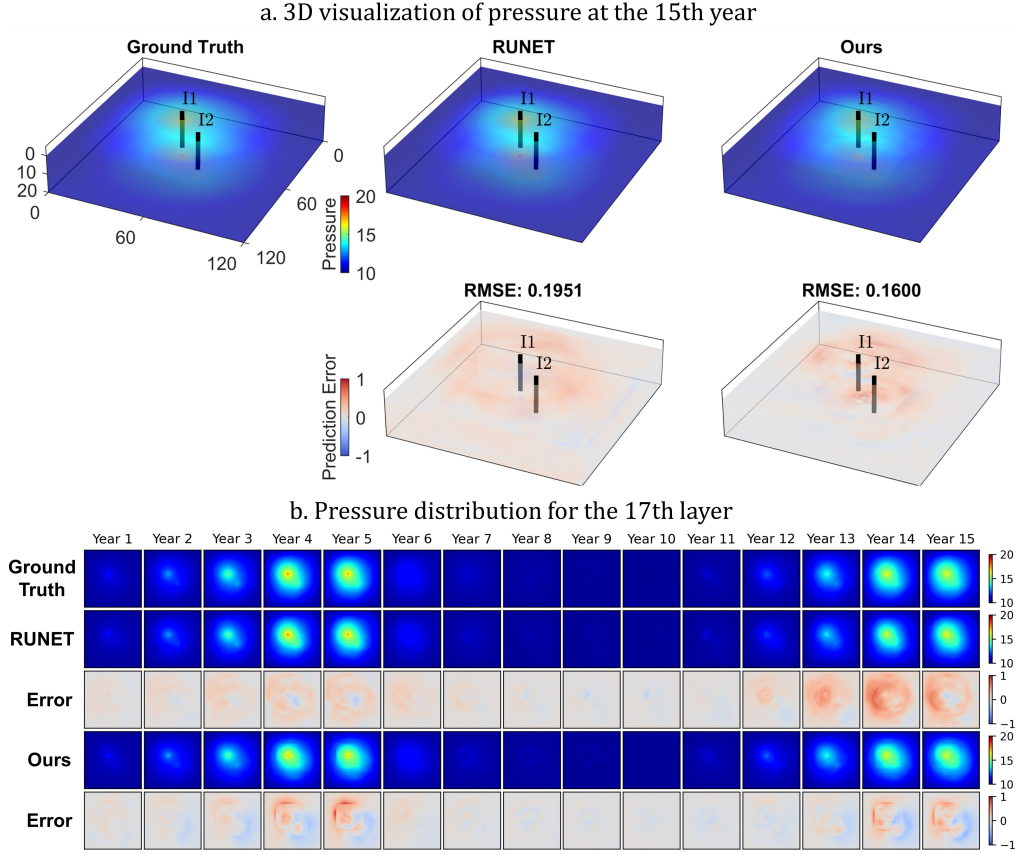


Figure 12: Visualization of pressure prediction over unseen control and permeability. The pressure values are measured in MPa, and the RMSE is also reported in MPa.

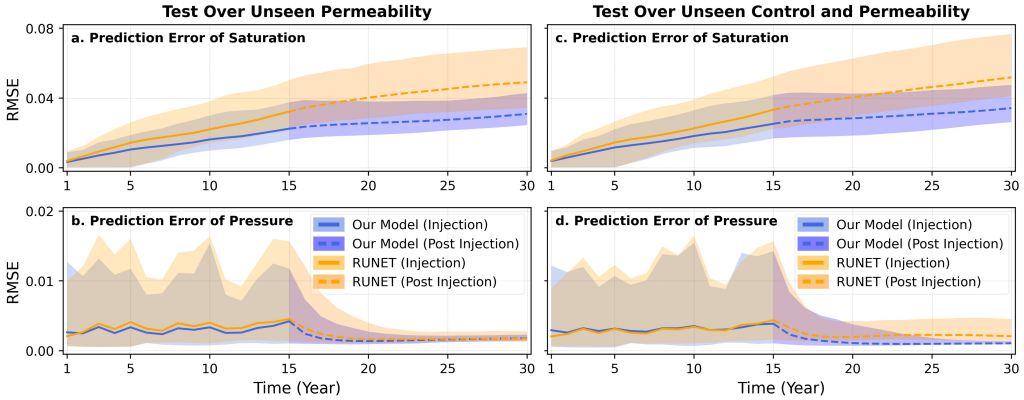


Figure 13: Prediction errors of normalized saturation and normalized pressure over injection and post-injection for the examples of (left) unseen permeability and (right) unseen control and permeability. The first 15 years denote the injection, while the last 15 years denote the post-injection where injection rates are zeros for two wells.

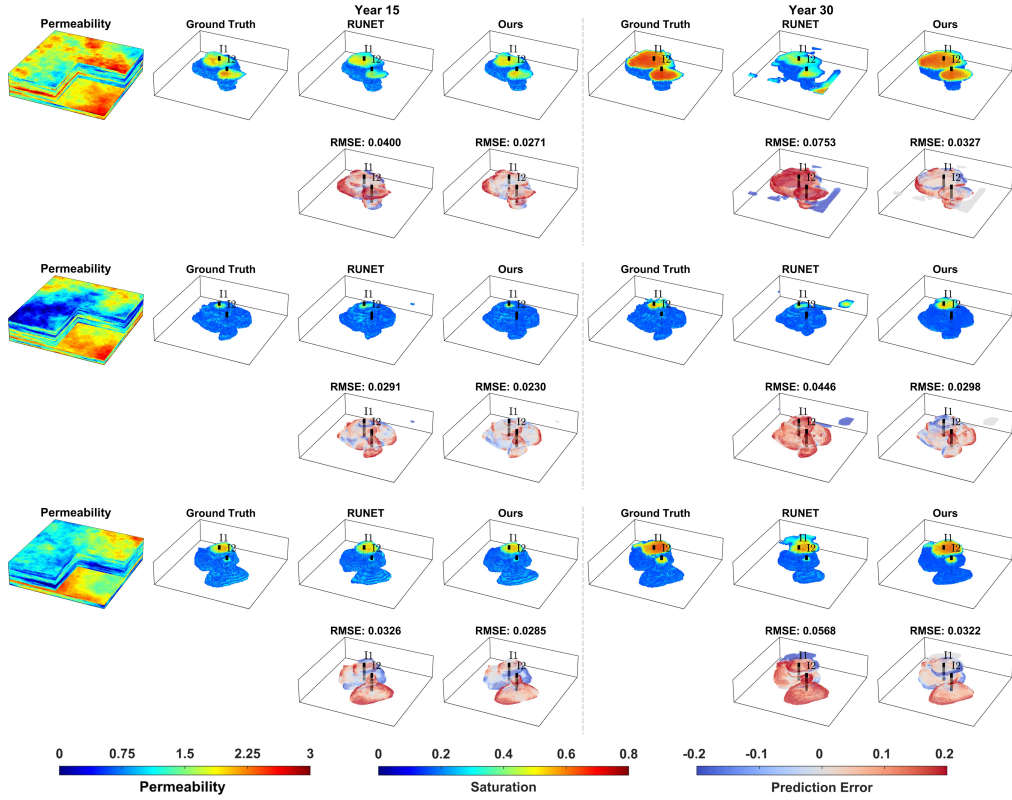


Figure 14: Visualization of saturation prediction of three different cases in the 15th and 30th years. Each case has different permeability and injection control as inputs. The permeability map is in the unit of  $\log_{10} (mD)$ .

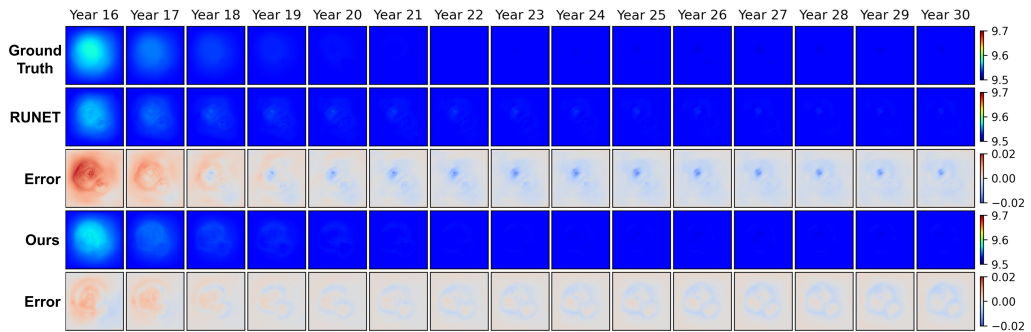


Figure 15: Visualization of pressure prediction over the post-injection period.

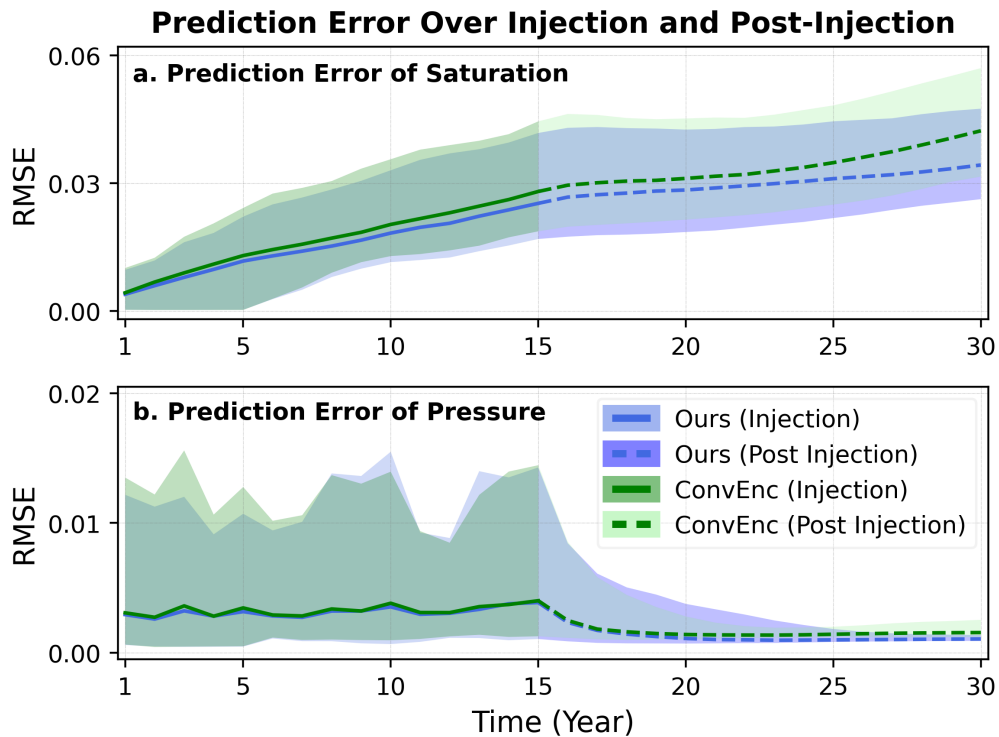


Figure 16: Prediction errors of normalized saturation and normalized pressure over injection and post-injection for two predictive models with different encoders: convolutional and physics-based.

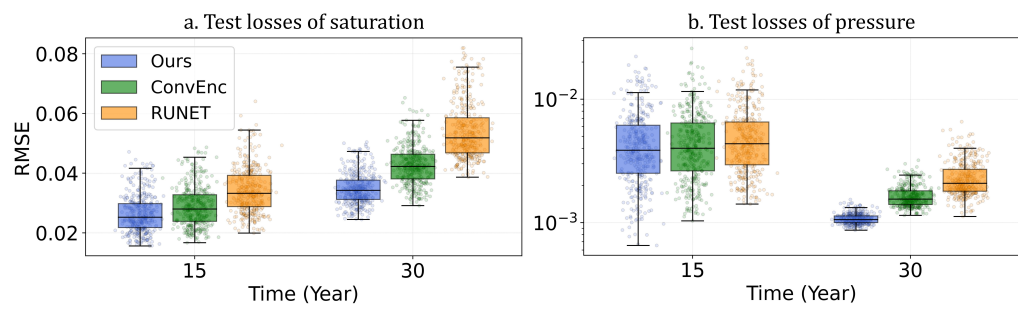


Figure 17: Distributions of test losses of (a) saturation and (b) pressure for different models.

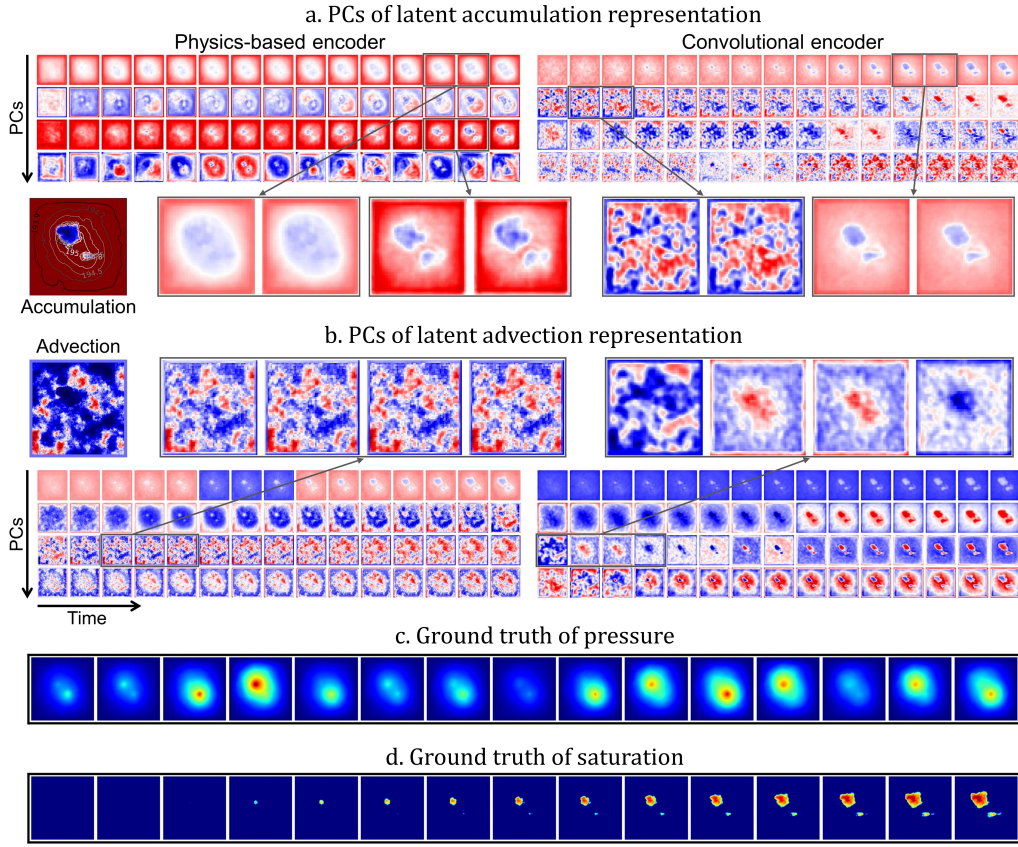


Figure 18: Visualization of the first four principal components of latent representations of (a) accumulation and (b) advection terms from two deep learning models with physics-based (left column) and convolutional encoders (right column), respectively. Each row in (a) and (b) represents the evolution of a principal component over the first 15 years. (c) and (d) visualize the ground truths of pressure and saturation of the first layer over the first 15 years. The true accumulation and z-direction advection of the wetting phase are provided in (a) and (b) for reference.

755

## Tables

756 **Acknowledgement**

757 The authors acknowledge the support provided by Energi Simulation through an  
758 Industrial Research Chair on Subsurface Energy Data Science at USC. Upon publica-  
759 tion of this study, a link to the data, codes, and examples used in this study will be posted  
760 to the FAIR-compliant Zenodo online repository as well as our research website at <http://sees.usc.edu>.

761 **Author Contribution**

762 **Zhen Qin:** Conceptualization, Methodology, Software, Data curation, Investigation,  
763 Validation, Visualization, Writing - Original draft preparation. **Yingxiang Liu:**  
764 Conceptualization, Data curation, Investigation, Validation. **Fangning Zheng:** Soft-  
765 ware, Data curation, Visualization, Writing- Original draft preparation. **Behnam Ja-**  
766 **farpour:** Conceptualization, Resources, Supervision, Funding acquisition, Writing - Re-  
767 view & Editing.

## 768 Appendix A Governing Equations

769 We follow the work in (Voskov, 2017) to derive governing equations and implement  
 770 the finite-volume discretization for the mass balance equation. For a system with  $n_c$  com-  
 771 ponents and  $n_p$  phases, the transport equations can be written as follows:

$$\frac{\partial}{\partial t} \left( \phi \sum_{\xi=1}^{n_p} x_{i,\xi} \rho_\xi S_\xi \right) + \nabla \cdot \sum_{\xi=1}^{n_p} (x_{i,\xi} \rho_\xi \mathbf{v}_\xi) = \sum_{\xi=1}^{n_p} x_{i,\xi} \rho_\xi \tilde{q}_\xi, \quad i = 1, \dots, n_c, \quad (\text{A1})$$

772 where  $\phi$  is porosity;  $x_{i,\xi}$  is the mole fraction of component  $i$  in phase  $\xi$ ;  $\rho_\xi$  is the den-  
 773 sity of phase  $\xi$ ;  $S_\xi$  is the saturation of phase  $\xi$ ;  $\mathbf{v}_\xi$  is the volumetric flux vector (or Darcy  
 774 flux) for phase  $\xi$ ;  $\tilde{q}_\xi$  is the external sources or sinks of volumetric rate per unit volume  
 775 in phase  $\xi$ .

776 For a geologic CO<sub>2</sub> storage site where CO<sub>2</sub> is injected into the deep saline aquifer,  
 777 the phases  $\xi \in \{w, n\}$  could be  $w$  for the wetting phase (brine) and  $n$  for the non-wetting  
 778 phase (supercritical CO<sub>2</sub>). The multiphase extension of Darcy's equation is applied to  
 779 describe the flow of each phase and is written as:

$$\mathbf{v}_\xi = -\mathbf{K} \frac{k_{r,\xi}}{\mu_\xi} (\nabla p_\xi - \rho_\xi g \nabla d) = -\lambda_\xi \mathbf{K} (\nabla p_\xi - \rho_\xi g \nabla d), \quad \xi \in \{w, n\}, \quad (\text{A2})$$

780 where  $\mathbf{K}$  is the permeability tensor,  $k_{r,\xi}$  is the relative permeability,  $\mu_\xi$  is the phase vis-  
 781 cosity,  $\lambda_\xi = k_{r,\xi}/\mu_\xi$  is the phase mobility,  $p_\xi$  is the phase pressure,  $g$  is the gravitational  
 782 acceleration, and  $d$  represents the depth.

783 The capillary pressure is defined as the difference between the pressure of two phases  
 784 and is a function of saturation:

$$p_c(s_w) = p_n - p_w, \quad (\text{A3})$$

785 where  $p_n$  and  $p_w$  are the pressures of non-wetting ( $n$ ) and wetting phases ( $w$ ).

786 By applying the finite-volume discretization and backward Euler approximation  
 787 in time, the mass balance equation can be discretized as:

$$V \left( (\phi \sum_{\xi=1}^{n_p} x_{i,\xi} \rho_\xi S_\xi)^{(n+1)} - (\phi \sum_{\xi=1}^{n_p} x_{i,\xi} \rho_\xi S_\xi)^{(n)} \right) \\ - \Delta t \sum_{l \in L} \left( \sum_{\xi=1}^{n_p} x_{i,\xi}^l \rho_\xi^l T_\xi^l \Delta \psi_\xi^l \right) + \Delta t \sum_{\xi=1}^{n_p} x_{i,\xi} \rho_\xi q_\xi = 0, \quad (\text{A4})$$

788 where  $V$  is the volume of the grid cell;  $T_\xi^l$  is the phase transmissibility between two grid  
 789 cells connected by the interface  $l$ ;  $\Delta \psi_\xi^l$  is the phase potential difference across the inter-  
 790 face  $l$  considering pressure, capillary pressure, and gravity;  $q_\xi$  is the volumetric rate of  
 791 phase  $\xi$ .

792 In this work, we simplify the CO<sub>2</sub>-brine system to an immiscible two-fluid-phase  
 793 system with no internal component gradient. Then the mass balance equation reduces  
 794 to the phase-base balance equation, written as:

$$\frac{\partial}{\partial t} (\phi S_\xi \rho_\xi) + \nabla \cdot (\rho_\xi \mathbf{v}_\xi) = \rho_\xi \tilde{q}_\xi, \quad \xi \in \{w, n\}. \quad (\text{A5})$$

795 The discretized mass balance equation in Eq. A4 is then transformed into:

$$V ((\phi \rho_\xi S_\xi) - (\phi \rho_\xi S_\xi)^t) - \Delta t \sum_{l \in L} \rho_\xi^l T_\xi^l \Delta \psi_\xi^l = \Delta t \rho_\xi q_\xi. \quad (\text{A6})$$

796 For the two grid cells  $u$  and  $v$  with the interface of  $l$ ,  $T_\xi^l$  is defined as follows:

$$T_\xi^l = \frac{\bar{k}_{u,v} A_l}{L_{u,v}} \lambda_\xi = T_m \lambda_\xi, \quad (\text{A7})$$

797 where  $\bar{k}_{u,v}$  is the harmonic average of permeability between the grid cells  $u$  and  $v$ ;  $A_l$   
 798 is the area of interface  $l$ ;  $L_{u,v}$  is the distance between the grid cells  $u$  and  $v$ .

799 The porosity  $\phi$  in can be represented as  $\phi_0(1 + c_r(p - p_{ref}))$ . By denoting  $1 +$   
 800  $c_r(p - p_{ref})$  as  $c_\phi$ , Eq. A6 can be written as:

$$((c_\phi \rho_\xi S_\xi) - (c_\phi \rho_\xi S_\xi)^t) - \frac{\Delta t}{V \phi_0} \sum_{l \in L} \rho_\xi^l \lambda_\xi^l T_m^l \Delta \psi_\xi^l = \frac{\Delta t}{V \phi_0} \rho_\xi q_\xi. \quad (\text{A8})$$

801 By presenting the Eq. (A8) in algebraic form and the definition in Eqs. (4 - 9), Eq.  
 802 (A8) can be rewritten as follows:

$$\begin{aligned} r_\xi(\mathbf{x}, \mathbf{m}, \mathbf{u}^t) = \\ (\mathbf{z}_{acc,\xi}(\mathbf{x}) - \mathbf{z}_{acc,\xi}(\mathbf{x}^t)) - \mathbf{z}_{adv,\xi}(\mathbf{x}, \mathbf{m}) + \mathbf{z}_{src,\xi}(\mathbf{x}, \mathbf{u}) = \mathbf{0}. \end{aligned} \quad (\text{A9})$$

803 **Appendix B Implementation Details**

804 **B1 Description of Decoder and Control Encoder**

805 At each time step  $t$ , the control encoder takes the control variable  $\mathbf{u}^t$  as input and  
 806 generates the latent variable  $\mathbf{z}_{src}^t$  as output. The control encoder consists of two 3D con-  
 807 volutional (Conv3D) layers with linear activation functions and a kernel size of 3 on x-  
 808 , y-, and z-directions. The output from Conv3D layers is downsampled by reducing the  
 809 spatial dimension by a factor of 2 and projected to the latent space with the feature di-  
 810 mension of  $d_l$ .

811 At each time step  $t$ , the decoder takes the latent variables  $\mathbf{z}_{acc}^t$  and  $\mathbf{z}_{adv}^t$  as well  
 812 as the static variable  $\mathbf{m}$  as inputs and generates the dynamic states  $\mathbf{S}_n^t$  and  $\mathbf{p}^t$  as out-  
 813 puts (Figure B1). First, the latent variables from the processor layer are projected back  
 814 to the original dimension  $D$  through the upsampling layers. Second, the inputs to the  
 815 decoder are projected to the space with the dimension of  $d_{d_1}$  for each grid block. The  
 816 projected features are then fused together to be the variable  $\mathbf{z}^t$  through addition and  
 817 concatenation. The role of the input  $\mathbf{m}$  here is to remove the effect of static variables,  
 818  $\mathbf{T}_m$  and  $\mathbf{I}_{PV}$ , that are coupled in the latent variable  $\mathbf{z}_{adv}^t$ . Then, the dynamic variable  
 819  $\mathbf{x}^t = \{\mathbf{p}^t, \mathbf{S}_n^t\}$  is learned from the latent variable  $\mathbf{z}^t$  through two Conv3D layers with  
 820 the dimension of output channels to be  $d_{d_2}$  and  $d_{d_3}$ , respectively.

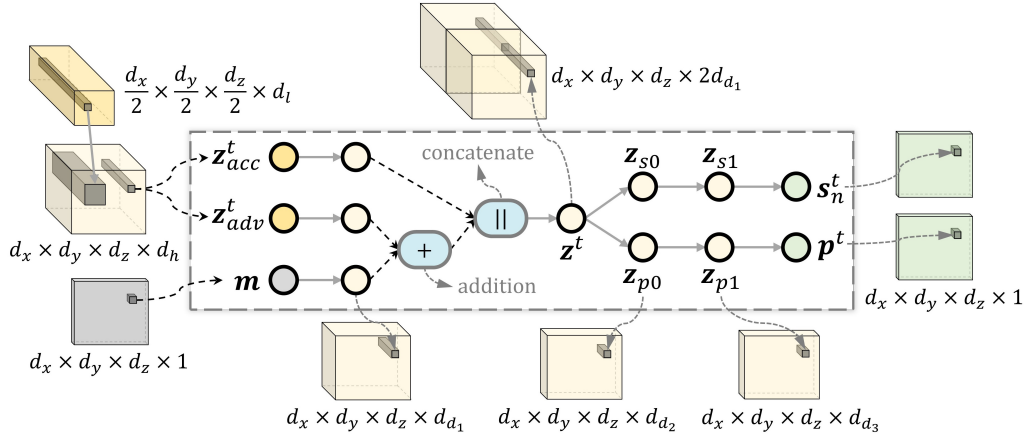


Figure B1: Illustration of the architecture of the decoder.

821            **B2 Hyperparameters of Deep Learning Models**

822        The hyperparameters of deep learning models, including our proposed model and  
 823        the modified Recurrent R-U-Net are summarized in Tables B1 and B2. Both two mod-  
 824        els consist of approximately 3 million trainable parameters.

Table B1: Hyperparameters of each module of the proposed model: Encoder, Processor, and Decoder. The third column denotes the selected values of hyperparameters. The last column denotes the feasible range of the hyperparameters.

Module	Hyperparameters	Value	Range
Encoder	Physical Operator Dimension, $d_o$	40	{10, 20, 30, 40}
	Hidden Dimension, $d_h$	16	{8, 12, 16, 20}
	Latent Dimension, $d_l$	32	{24, 32, 48}
Processor	Dimension of Residual Feature, $d_r$	48	{32, 48, 64}
	Number of Residual Layers, $N_{rl}$	3	{2, 3, 4}
Decoder	Dimension of the 1 <sup>st</sup> Layer, $d_{d_1}$	16	{8, 16, 32}
	Dimension of the 2 <sup>nd</sup> Layer, $d_{d_2}$	8	{4, 8, 12, 16}
	Dimension of the 3 <sup>rd</sup> Layer, $d_{d_3}$	4	{4, 6, 8}

Table B2: Hyperparameters of modified Recurrent R-U-Net.

Hyperparameter	Selected Size
Channels	[16, 32, 64]
# of Groups for GroupNorm Layer	4

825 **B3 Configuration of Training**

826 The training in this study employs the Adam optimizer as the chosen optimization  
 827 algorithm, with the decay of the learning rate implemented gradually. Specifically,  
 828 the learning rate decreases progressively over every step size of training samples by be-  
 829 ing multiplied by the decay factor. Further details about the optimization hyperparam-  
 830 eters can be found in Table B3. The number of samples used for training, validation, and  
 831 test sets for all models and experiments are tabulated in Table B4. All experiments are  
 832 implemented using PyTorch (Paszke et al., 2019) and conducted on a single NVIDIA A100  
 833 40GB GPU. Summaries of model efficiency comparison and the input configuration are  
 834 presented in Tables B5 and B6, respectively. As shown in the input configuration, the  
 835 first dimension of three variables denotes the batch size of 1. The second and third di-  
 836 mensions of the control variable are the number of time steps of the prediction horizon  
 837 during training and the number of components (water and CO<sub>2</sub>), respectively. The sec-  
 838 ond dimension of the dynamic variable denotes the number of dynamic variables includ-  
 839 ing pressure and saturation. The second dimension of static variable represents the num-  
 840 ber of static variables, including the inverse of grid volume, depth, and transmissibility  
 841 of six faces over  $x$ -,  $y$ -, and  $z$ -directions for a structured grid system. The dimension  $128 \times$   
 842  $128 \times 20$  represents the grid sizes of the reservoir over three directions.

Table B3: Hyperparameters for the training of our model and RUNET in all experiments.

Hyperparameter	Value
Batch Size	2
Learning Rate	1e-4
Step Size	4500
Decay Factor	0.9
Gradient Clipping	40

Table B4: The numbers of samples used for training, validating, and testing all models in three experiments.

Experiment	Training	Validate	Test
Exp 1 (Public Dataset)	200, 500, 1000, 1500, 2000, 2500	50	373
Exp 1 (Our Dataset)	700	100	200
Exp 2	700	100	200

Table B5: Comparison of model efficiency. ConvEnc refers to the model sharing the same architecture as the proposed DL model except the encoder is the convolutional encoder.

Model	Parameter (Million)	Runtime (s/iter)
Ours	3.3951	0.2238
RUNET	3.0371	0.4201
ConvEnc	3.5225	0.4012

Table B6: Input size used for the comparison of model efficiency.

Input Variable	Input Size
Control Variable	$1 \times 8 \times 2 \times 128 \times 128 \times 20$
Dynamic Variable	$1 \times 2 \times 128 \times 128 \times 20$
Static Variable	$1 \times 8 \times 128 \times 128 \times 20$

## 843 Appendix C Numerical Simulation Model and Data Generation

844 In this section, we describe the numerical simulation model used to generate the  
 845 training and test data for the described physics-encoded DL model for predicting the spatial-  
 846 temporal evolution of the pressure and saturation for subsurface CO<sub>2</sub> storage. Figure  
 847 C1 shows a synthetic 3D two-phase flow simulation model constructed using CMG-GEM  
 848 (Computer Modeling Group (CMG), 2019). The storage reservoir region is encompassed  
 849 by an aquifer region used to allow pressure dissipation and minimize the effects of no-  
 850 flow boundaries. The zero-flux boundary conditions are imposed on the reservoir bound-  
 851 boundaries. The storage reservoir is at a depth of 1000 meters with a vertical grid dimension  
 852 of 20 grid blocks × 2.5 meters and a horizontal grid dimension of 120 grid blocks × 50  
 853 meters, resulting in a total grid number of 288,000. The aquifer region is situated at the  
 854 same depth and exhibits identical vertical and horizontal resolutions for the middle sec-  
 855 tion as the storage reservoir. The two sides of the horizontal resolutions of the aquifer  
 856 region are coarsened to 4 grid blocks × 500 meters to reduce computational cost. The  
 857 total grid number of the entire simulation model is 327,680. The reservoir region has het-  
 858 erogeneous permeability values ranging from 0.1 to 2000 mD. Table C1 summarizes the  
 859 simulation model settings. The injection spans 15 years, followed by a monitoring pe-  
 860 riod of 85 years without CO<sub>2</sub> injection.

861 In this paper, we assume an isothermal environment for the CO<sub>2</sub> injection and stor-  
 862 age processes. Various trapping mechanisms of CO<sub>2</sub> storage, including geologic, resid-  
 863 ual, solubility, and mineral trapping (Blunt, 2010), are considered in the simulation model.  
 864 We use the Brooks-Corey relative permeability model (Brooks, 1965) with  $n = 2$  to cal-  
 865 culate the CO<sub>2</sub>-water relative permeability. The maximum residual gas saturation ( $S_{grmax}$ )  
 866 is set to be 0.4. The capillary pressure for the sand-CO<sub>2</sub>-brine system is referred to Plug  
 867 and Bruining (2007) of the drainage capillary pressure curve for supercritical CO<sub>2</sub> at 40  
 868 °C. The gas density is calculated with the Peng-Robinson Equation of State (Peng & Robin-  
 869 son, 1976). The gas viscosity is calculated from the Jossi, Stiel and Thodos correlation  
 870 (Poling et al., 2001). The aqueous phase density and viscosity are calculated from the  
 871 Rowe and Chou correlation (Rowe Jr & Chou, 1970) and the Kestin correlation (Kestin  
 872 et al., 1981), respectively.

873 Uncertainties in the geologic properties of storage reservoirs, particularly in CO<sub>2</sub>  
 874 sequestration sites like saline aquifers, arise due to limited understanding and measure-  
 875 ment of geologic representation at various scales (Ma, 2011). These uncertainties stem  
 876 from factors such as reservoir heterogeneity, anisotropy, and lateral variation resulting  
 877 from uncertain rock composition, texture, pore structure, and rock type, which can in-  
 878 fluence the stress state and strength differences within the rocks (Middleton et al., 2012).  
 879 Consequently, geomechanical properties become uncertain, impacting the capacity and  
 880 costs of CO<sub>2</sub> storage in carbon capture and storage systems during pre-injection, injec-  
 881 tion, and post-injection periods (Anderson, 2017). To enhance the robustness of the de-  
 882 veloped deep learning model and effectively address geologic uncertainty, we employ sam-  
 883 pling techniques and ensemble representations. These techniques allow us to incorpo-  
 884 rate varying levels of heterogeneity range and generate multiple realizations of the per-  
 885 meability map. We utilize sequential Gaussian simulation with the Stanford Geostatis-  
 886 tical Modeling Software (Remy et al., 2009) for this purpose. The geometric anisotropy  
 887 is characterized by a spherical variogram model where the maximum (x-direction) and  
 888 medium (y-direction) ellipsoid ranges are set isotropically with three distinct scenarios  
 889 of 20, 60, and 100 units. The minimum ellipsoid range is represented by two distinct sce-  
 890 narios, namely 2 and 5 units. Consequently, a comprehensive set of six scenarios, each  
 891 featuring different ellipsoid ranges, is utilized to generate a total of 100 realizations per  
 892 scenario, thereby resulting in a total of 600 realizations of the 3D permeability maps. Fig-  
 893 ure C2 shows the permeability maps of the first four realizations from each of the six dis-  
 894 tinct scenarios.

Given each realization of the permeability map, the simulation data is generated based on various cases of well injection schedules. The well location is fixed at 64,64,17 for the one-well scenario and the well indexes of the two-well scenario are fixed at {55,55,17} and {75,75,17}. The total CO<sub>2</sub> injection volume,  $V_{T_{CO_2}}^{inj}$ , over 15 years of injection is fixed to be  $3.5e+09 m^3$  ( $\sim 10 mtCO_2$ ) for both one-well and two-well scenarios. To ensure comprehensive coverage of the realistic response space, we divide the injection duration into three intervals, each spanning 5 years. We assign each interval with an injection volume,  $V_{interval_x}$ , with one of the  $V_{high}$ ,  $V_{med}$ , or  $V_{low}$ , where  $V_{high} = 0.5V_{T_{CO_2}}^{inj}$ ,  $V_{med} = 0.35V_{T_{CO_2}}^{inj}$ , and  $V_{low} = 0.15V_{T_{CO_2}}^{inj}$ . We then create ten different combinations of those injection volumes as shown in Table C2 and Figure C3 (a). The injection rate,  $u$  ( $m^3/day$ ), changes every year, and  $U = \{u^{t_1}, u^{t_2}, \dots, u^{t_k}\}$  where  $k = 15$ . We randomly assign a portion of the injection volume to each year based on its corresponding interval. Let

$$p = rand(1, 5) = [p_1, p_2, p_3, p_4, p_5], \quad (C1)$$

and injection rate  $u$  at time  $t_i$  is calculated by

$$u^{t_i} = \frac{p_i}{sum(p)} \frac{V_{interval_x}}{365}, \quad (C2)$$

where  $p_i$  corresponds to the same injection interval  $x$  where  $u^{t_i}$  belongs to.

Figure C3 (b) shows an example of random injection rate allocation based on total injection allocation in Figure C3 (a). In this way, a total of 6000 simulation runs are performed and the spatial and temporal results of pressure and gas saturation are generated. The described data generation approach maximizes our ability to explore a wide range of injection rate combinations.

For the two-well scenario, the injection rate is distributed into two wells with specific portions:

$$[u_{w_1}^{t_i}, u_{w_2}^{t_i}] = u^{t_i} [q_i, 1 - q_i], \quad (C3)$$

where  $q_i$  is the percentage of injection amount assigned to well 1,  $(1-q_i)$  is the percentage of injection amount assigned to well 2, and  $q = [0.1 : 0.1 : 1]$  for a total of 10 injection schedules for each permeability realization.

Table C1: Numerical simulation model settings.

	Reservoir Region	Aquifer Region
Grid numbers $\times$ Grid size (meter) in $x$ and $y$	$30 \times 100$	$4 \times 500 + 30 \times 100 + 4 \times 500$
Grid numbers $\times$ Grid size (meter) in $z$	$20 \times 2.5$	$20 \times 2.5$
Permeability (mD)	$0.1 - 2000$	200
Porosity	0.18	0.18
Pore pressure gradient (kPa/m)	9.8	9.8
$k_v/k_h$	0.1	0.1
Temperature ( $^{\circ}\text{C}$ ) (isothermal condition)	40	40

Table C2: Ten combinations of the percentage injection volume for each interval.  $V_{high}$ ,  $V_{med}$ ,  $V_{low}$ , and  $V_{avg}$  correspond to 50%, 35%, 15%, and 33.33% of the total injection volume, respectively.

	$V_{interval_1}$	$V_{interval_2}$	$V_{interval_3}$
Combination 1	$V_{high}$	$V_{med}$	$V_{low}$
Combination 2	$V_{high}$	$V_{low}$	$V_{med}$
Combination 3	$V_{med}$	$V_{high}$	$V_{low}$
Combination 4	$V_{med}$	$V_{low}$	$V_{high}$
Combination 5	$V_{low}$	$V_{high}$	$V_{med}$
Combination 6	$V_{low}$	$V_{med}$	$V_{high}$
Combination 7	$V_{avg}$	$V_{avg}$	$V_{avg}$
Combination 8	$V_{high}$	0	$V_{high}$
Combination 9	$V_{high}$	$V_{high}$	0
Combination 10	0	$V_{high}$	$V_{high}$

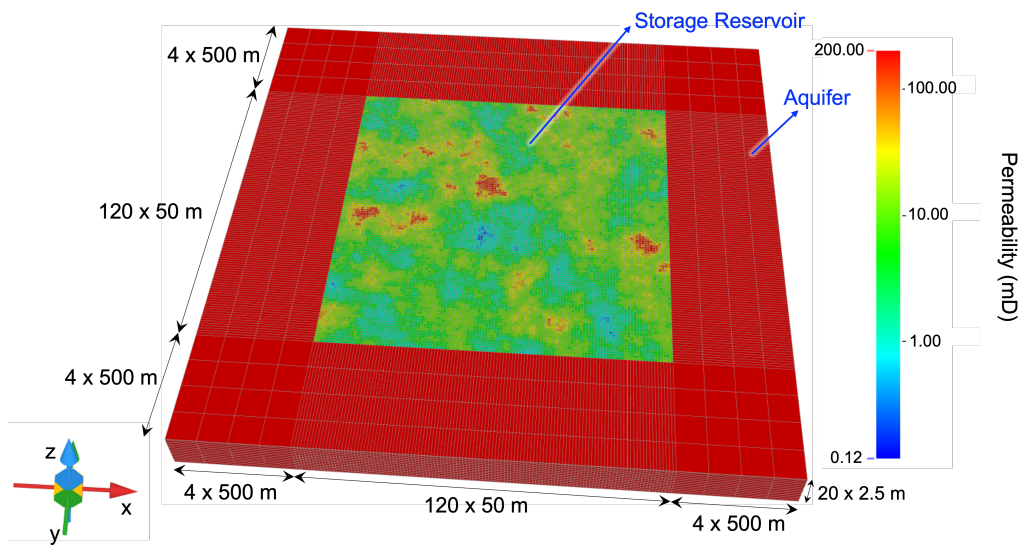


Figure C1: Numerical simulation model of 3D deep saline aquifer reservoir.

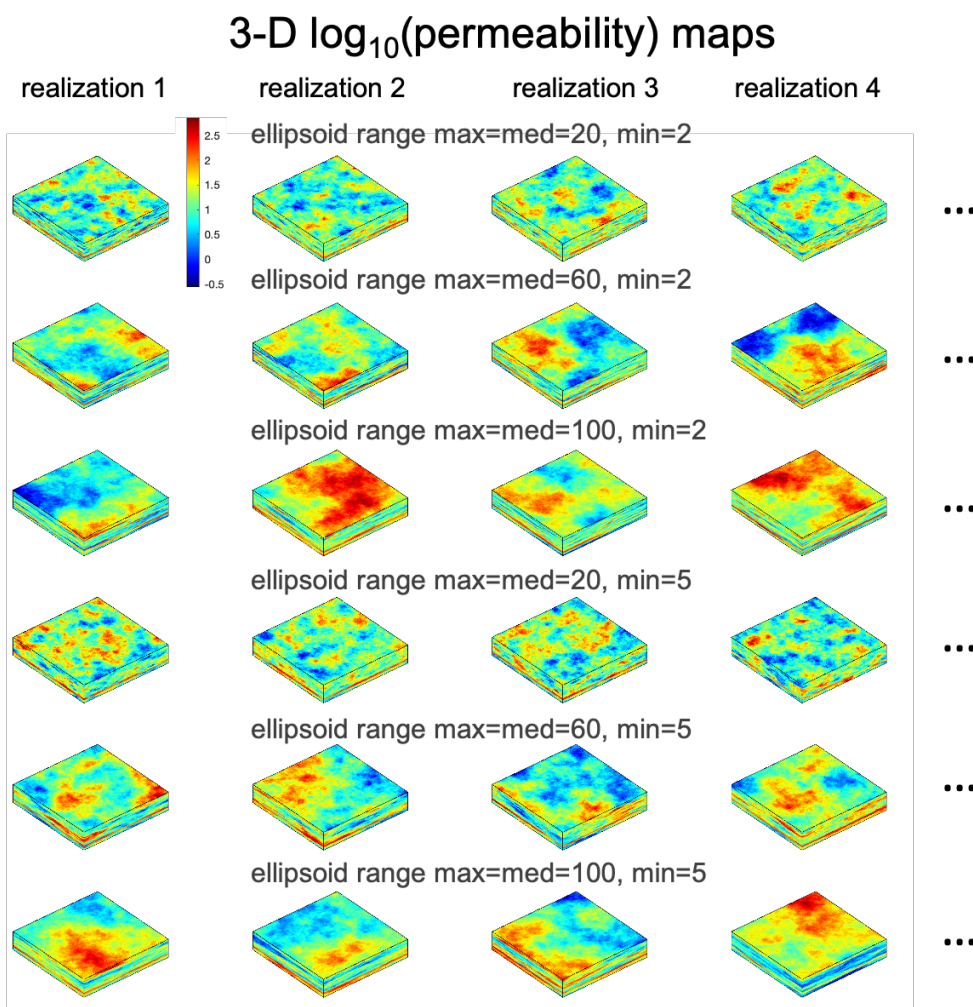


Figure C2: The 3D Permeability maps of the first four realizations from each of the six scenarios with distinct ellipsoid ranges.

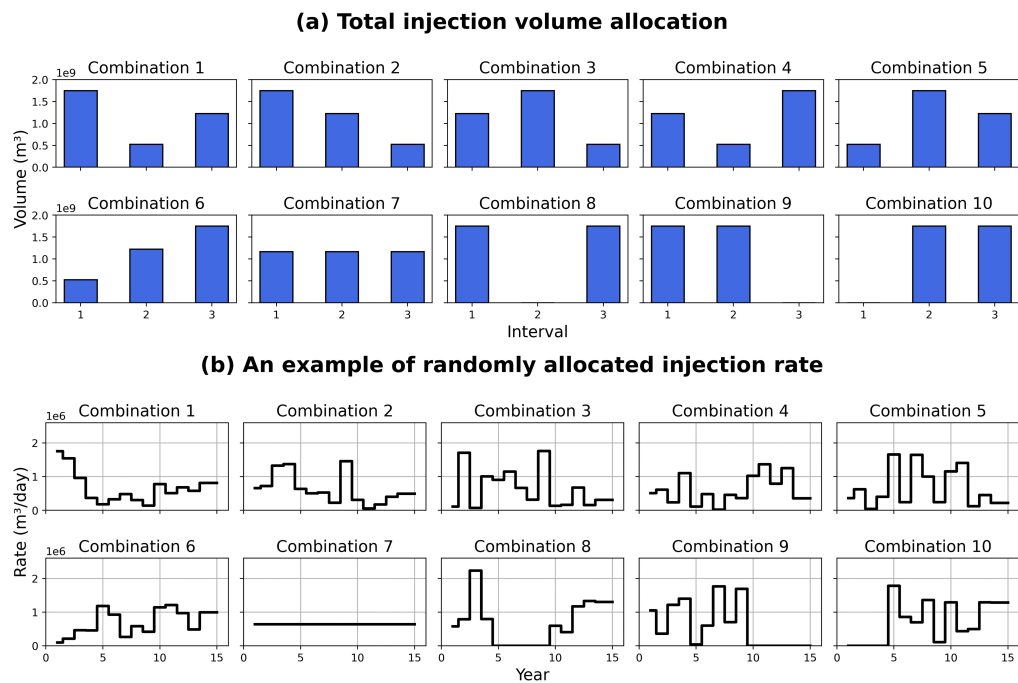


Figure C3: Ten combinations of the percentage injection volume for each interval. (a) total injection volume allocation for each interval. (b) an example of random injection rate allocation based on total injection allocation on (a).

919 **References**

- 920 Ajayi, T., Gomes, J. S., & Bera, A. (2019). A review of CO<sub>2</sub> storage in geological formations emphasizing modeling, monitoring and capacity estimation approaches. *Petroleum Science*, 16(5), 1028–1063. doi: 10.1007/s12182-019-0340-8
- 921 Anderson, S. T. (2017). Cost implications of uncertainty in CO<sub>2</sub> storage resource estimates: A review. *Natural Resources Research*, 26, 137–159.
- 922 Bandilla, K. W., Celia, M. A., Birkholzer, J. T., Cihan, A., & Leister, E. C. (2015). Multiphase modeling of geologic carbon sequestration in saline aquifers. *Groundwater*, 53, 362–377. doi: 10.1111/gwat.12315
- 923 Blunt, M. (2010). Carbon dioxide storage. *Grantham Institute Briefing Paper*, 4.
- 924 Brooks, R. H. (1965). *Hydraulic properties of porous media*. Colorado State University.
- 925 Bui, M., Adjiman, C. S., Bardow, A., Anthony, E. J., Boston, A., Brown, S., ... Mac Dowell, N. (2018). Carbon capture and storage (CCS): the way forward. *Energy & Environmental Science*, 11, 1062–1176. doi: 10.1039/C7EE02342A
- 926 Celia, M. A., Bachu, S., Nordbotten, J. M., & Bandilla, K. W. (2015). Status of CO<sub>2</sub> storage in deep saline aquifers with emphasis on modeling approaches and practical simulations. *Water Resources Research*, 51, 6846–6892. doi: 10.1002/2015WR017609
- 927 Chen, R. T. Q., Rubanova, Y., Bettencourt, J., & Duvenaud, D. K. (2018). Neural Ordinary Differential Equations. In *Advances in Neural Information Processing Systems* (Vol. 31, pp. 6571–6583). Curran Associates, Inc.
- 928 Computer Modeling Group (CMG). (2019). *Gem user manual*.
- 929 Cuomo, S., Di Cola, V. S., Giampaolo, F., Rozza, G., Raissi, M., & Piccialli, F. (2022). Scientific machine learning through physics-informed neural networks: Where we are and what's next. *Journal of Scientific Computing*, 92(3), 88.
- 930 Dulny, A., Hotho, A., & Krause, A. (2022). NeuralPDE: Modelling Dynamical Systems from Data. In *KI 2022: Advances in Artificial Intelligence* (pp. 75–89). Springer International Publishing.
- 931 E, W. (2017). A proposal on machine learning via dynamical systems. *Communications in Mathematics and Statistics*, 1(5), 1–11. doi: 10.1007/s40304-017-0103-z
- 932 E, W., Han, J., & Jentzen, A. (2017). Deep learning-based numerical methods for high-dimensional parabolic partial differential equations and backward stochastic differential equations. *Communications in Mathematics and Statistics*, 5(4), 349–380. doi: 10.1007/s40304-017-0117-6
- 933 Faroughi, S. A., Pawar, N., Fernandes, C., Raissi, M., Das, S., Kalantari, N. K., & Mahjour, S. K. (2023). *Physics-Guided, Physics-Informed, and Physics-Encoded Neural Networks in Scientific Computing*. arXiv. (arXiv:2211.07377 [cs]) doi: 10.48550/arXiv.2211.07377
- 934 Fuks, O., & Tchelepi, H. A. (2020). Limitations of physics informed machine learning for nonlinear two-phase transport in porous media. *Journal of Machine Learning for Modeling and Computing*, 1(1), 19–37. doi: 10.1615/JMachLearnModelComput.2020033905
- 935 Gorecki, C. D., Ayash, S. C., Liu, G., Braunerger, J. R., & Dotzenrod, N. W. (2015). A comparison of volumetric and dynamic CO<sub>2</sub> storage resource and efficiency in deep saline formations. *International Journal of Greenhouse Gas Control*, 42, 213–225. doi: 10.1016/j.ijggc.2015.07.018
- 936 He, K., Zhang, X., Ren, S., & Sun, J. (2016, June). Deep residual learning for image recognition. In *Proceedings of the ieee conference on computer vision and pattern recognition (cvpr)* (pp. 770–778).
- 937 Hendrycks, D., & Gimpel, K. (2023). *Gaussian error linear units (gelus)*.
- 938 Ioffe, S., & Szegedy, C. (2015, 07–09 Jul). Batch normalization: Accelerating deep network training by reducing internal covariate shift. In *Proceedings of the*

- 974                   32nd international conference on machine learning (Vol. 37, pp. 448–456).  
 975                   Lille, France: PMLR.
- 976     J. Nagoor Kani, & Elsheikh, A. H. (2019). Reduced-order modeling of subsurface  
 977                   multi-phase flow models using deep residual recurrent neural networks. *Trans-*  
 978                   *port in Porous Media*, 126(3), 713–741. doi: 10.1007/s11242-018-1170-7
- 979     Jiang, X. (2011). A review of physical modelling and numerical simulation of long-  
 980                   term geological storage of CO<sub>2</sub>. *Applied Energy*, 88(11), 3557–3566. doi: 10  
 981                   .1016/j.apenergy.2011.05.004
- 982     Jiang, Z., Tahmasebi, P., & Mao, Z. (2021). Deep residual u-net convolution  
 983                   neural networks with autoregressive strategy for fluid flow predictions in  
 984                   large-scale geosystems. *Advances in Water Resources*, 150, 103878. doi:  
 985                   10.1016/j.advwatres.2021.103878
- 986     Karniadakis, G. E., Kevrekidis, I. G., Lu, L., Perdikaris, P., Wang, S., & Yang, L.  
 987                   (2021). Physics-informed machine learning. *Nature Reviews Physics*, 3(6),  
 988                   422–440. doi: 10.1038/s42254-021-00314-5
- 989     Kestin, J., Khalifa, H. E., & Correia, R. J. (1981). Tables of the dynamic and kine-  
 990                   matic viscosity of aqueous nacl solutions in the temperature range 20–150 c  
 991                   and the pressure range 0.1–35 mpa. *Journal of physical and chemical reference*  
 992                   *data*, 10(1), 71–88.
- 993     Kolesnikov, A., Beyer, L., Zhai, X., Puigcerver, J., Yung, J., Gelly, S., & Houlsby,  
 994                   N. (2020). Big transfer (BiT): General visual representation learning. In  
 995                   A. Vedaldi, H. Bischof, T. Brox, & J.-M. Frahm (Eds.), *Computer Vision –*  
 996                   *ECCV 2020* (pp. 491–507). Cham: Springer International Publishing.
- 997     Krishnapriyan, A., Gholami, A., Zhe, S., Kirby, R., & Mahoney, M. W. (2021).  
 998                   Characterizing possible failure modes in physics-informed neural networks. In  
 999                   *Advances in neural information processing systems* (Vol. 34, pp. 26548–26560).  
 1000                   Curran Associates, Inc.
- 1001     Li, Z., Kovachki, N. B., Azizzadenesheli, K., Liu, B., Bhattacharya, K., Stuart,  
 1002                   A. M., & Anandkumar, A. (2020). Fourier neural operator for paramet-  
 1003                   ric partial differential equations. *CoRR, abs/2010.08895*. Retrieved from  
 1004                   <https://arxiv.org/abs/2010.08895>
- 1005     Long, Z., Lu, Y., & Dong, B. (2019). PDE-Net 2.0: Learning PDEs from data with  
 1006                   a numeric-symbolic hybrid deep network. *Journal of Computational Physics*,  
 1007                   399, 108925. doi: 10.1016/j.jcp.2019.108925
- 1008     Long, Z., Lu, Y., Ma, X., & Dong, B. (2018). PDE-Net: Learning PDEs from Data.  
 1009                   In *Proceedings of the 35th International Conference on Machine Learning* (pp.  
 1010                   3208–3216). PMLR.
- 1011     Lu, Y., Zhong, A., Li, Q., & Dong, B. (2018). Beyond finite layer neural net-  
 1012                   works: Bridging deep architectures and numerical differential equations. In  
 1013                   *Proceedings of the 35th International Conference on Machine Learning* (pp.  
 1014                   3276–3285). PMLR.
- 1015     Ma, Y. Z. (2011). Uncertainty analysis in reservoir characterization and manage-  
 1016                   ment: How much should we know about what we don't know? In *Uncer-*  
 1017                   *tainty Analysis and Reservoir Modeling* (pp. 1–15). American Association of  
 1018                   Petroleum Geologists. doi: 10.1306/13301404M963458
- 1019     Middleton, R. S., Keating, G. N., Viswanathan, H. S., Stauffer, P. H., & Pawar,  
 1020                   R. J. (2012). Effects of geologic reservoir uncertainty on CO<sub>2</sub> transport and  
 1021                   storage infrastructure. *International Journal of Greenhouse Gas Control*, 8,  
 1022                   132–142.
- 1023     Mo, S., Zabaras, N., Shi, X., & Wu, J. (2019). Deep autoregressive neural net-  
 1024                   works for high-dimensional inverse problems in groundwater contaminant  
 1025                   source identification. *Water Resources Research*, 55(5), 3856–3881. doi:  
 1026                   10.1029/2018WR024638
- 1027     Mo, S., Zhu, Y., Zabaras, N., Shi, X., & Wu, J. (2019). Deep convolutional encoder-  
 1028                   decoder networks for uncertainty quantification of dynamic multiphase flow

- in heterogeneous media. *Water Resources Research*, 55(1), 703–728. doi: 10.1029/2018WR023528
- Muther, T., Dahaghi, A. K., Syed, F. I., & Van Pham, V. (2023). Physical laws meet machine intelligence: current developments and future directions. *Artificial Intelligence Review*, 56(7), 6947–7013.
- Paszke, A., Gross, S., Massa, F., Lerer, A., Bradbury, J., Chanan, G., ... Chintala, S. (2019). Pytorch: An imperative style, high-performance deep learning library. In *Advances in neural information processing systems* (Vol. 32, pp. 8026–8037). Curran Associates, Inc.
- Pawar, R. J., Bromhal, G. S., Carey, J. W., Foxall, W., Korre, A., Ringrose, P. S., ... White, J. A. (2015). Recent advances in risk assessment and risk management of geologic CO<sub>2</sub> storage. *International Journal of Greenhouse Gas Control*, 40, 292–311. doi: 10.1016/j.ijggc.2015.06.014
- Peng, D. Y., & Robinson, D. B. (1976). A new two-constant equation of state. *Industrial & Engineering Chemistry Fundamentals*, 15(1), 59–64.
- Plug, W. J., & Bruining, J. (2007). Capillary pressure for the sand–CO<sub>2</sub>–water system under various pressure conditions. application to CO<sub>2</sub> sequestration. *Advances in Water Resources*, 30(11), 2339–2353.
- Poling, B. E., Prausnitz, J. M., & O'connell, J. P. (2001). *Properties of gases and liquids*. McGraw-Hill Education.
- Qin, Z., Jiang, A., Faulder, D., Cladouhos, T. T., & Jafarpour, B. (2023). Efficient optimization of energy recovery from geothermal reservoirs with recurrent neural network predictive models. *Water Resources Research*, 59(3), e2022WR032653. doi: <https://doi.org/10.1029/2022WR032653>
- Qin, Z., Jiang, A., Faulder, D., Cladouhos, T. T., & Jafarpour, B. (2024). Physics-Guided Deep Learning for Prediction of Energy Production from Geothermal Reservoirs. *Geothermics*, 116, 102824. doi: <https://doi.org/10.1016/j.geothermics.2023.102824>
- Rahaman, N., Baratin, A., Arpit, D., Draxler, F., Lin, M., Hamprecht, F., ... Courville, A. (2019, 09–15 Jun). On the spectral bias of neural networks. In *Proceedings of the 36th international conference on machine learning* (Vol. 97, pp. 5301–5310). PMLR.
- Raissi, M., Perdikaris, P., & Karniadakis, G. (2019). Physics-informed neural networks: A deep learning framework for solving forward and inverse problems involving nonlinear partial differential equations. *Journal of Computational Physics*, 378, 686–707. doi: 10.1016/j.jcp.2018.10.045
- Rao, C., Sun, H., & Liu, Y. (2021). Hard encoding of physics for learning spatiotemporal dynamics.
- Remy, N., Boucher, A., & Wu, J. (2009). *Applied geostatistics with sgems: A user's guide*. Cambridge University Press. Retrieved from <https://books.google.com/books?id=AFleg100LacC>
- Ronneberger, O., Fischer, P., & Brox, T. (2015). U-Net: Convolutional networks for biomedical image segmentation. In N. Navab, J. Hornegger, W. M. Wells, & A. F. Frangi (Eds.), *Medical image computing and computer-assisted intervention – miccai 2015* (pp. 234–241). Springer International Publishing.
- Rowe Jr, A. M., & Chou, J. C. (1970). Pressure-volume-temperature-concentration relation of aqueous sodium chloride solutions. *Journal of Chemical and Engineering Data*, 15(1), 61–66.
- Ruthotto, L., & Haber, E. (2020). Deep neural networks motivated by partial differential equations. *Journal of Mathematical Imaging and Vision*, 62(3), 352–364. doi: 10.1007/s10851-019-00903-1
- Shi, X., Chen, Z., Wang, H., Yeung, D.-Y., Wong, W.-k., & Woo, W.-c. (2015). Convolutional LSTM Network: A Machine Learning Approach for Precipitation Nowcasting. In C. Cortes, N. Lawrence, D. Lee, M. Sugiyama, & R. Garnett (Eds.), *Advances in Neural Information Processing Systems* (Vol. 28, p. 802—

- 1084 810). Curran Associates, Inc.
- 1085 Shokouhi, P., Kumar, V., Prathipati, S., Hosseini, S. A., Giles, C. L., & Kifer,  
1086 D. (2021). Physics-informed deep learning for prediction of CO<sub>2</sub> stor-  
1087 age site response. *Journal of Contaminant Hydrology*, 241, 103835. doi:  
1088 10.1016/j.jconhyd.2021.103835
- 1089 Tancik, M., Srinivasan, P., Mildenhall, B., Fridovich-Keil, S., Raghavan, N., Sing-  
1090 hal, U., ... Ng, R. (2020). Fourier features let networks learn high frequency  
1091 functions in low dimensional domains. In *Advances in neural information  
1092 processing systems* (Vol. 33, pp. 7537–7547). Curran Associates, Inc.
- 1093 Tang, H., Fu, P., Sherman, C. S., Zhang, J., Ju, X., Hamon, F., ... Morris, J. P.  
1094 (2021). A deep learning-accelerated data assimilation and forecasting work-  
1095 flow for commercial-scale geologic carbon storage. *International Journal of  
1096 Greenhouse Gas Control*, 112, 103488. doi: 10.1016/j.ijggc.2021.103488
- 1097 Tang, M., Ju, X., & Durlofsky, L. J. (2022). Deep-learning-based coupled flow-  
1098 geomechanics surrogate model for CO<sub>2</sub> sequestration. *International Journal of  
1099 Greenhouse Gas Control*, 118, 103692. doi: 10.1016/j.ijggc.2022.103692
- 1100 Tang, M., Liu, Y., & Durlofsky, L. J. (2020). A deep-learning-based surrogate model  
1101 for data assimilation in dynamic subsurface flow problems. *Journal of Compu-  
1102 tational Physics*, 413, 109456. doi: 10.1016/j.jcp.2020.109456
- 1103 Tang, M., Liu, Y., & Durlofsky, L. J. (2021). Deep-learning-based surrogate flow  
1104 modeling and geological parameterization for data assimilation in 3d sub-  
1105 surface flow. *Computer Methods in Applied Mechanics and Engineering*, 376,  
1106 113636. doi: 10.1016/j.cma.2020.113636
- 1107 Voskov, D. V. (2017). Operator-based linearization approach for modeling of mul-  
1108 tiphase multi-component flow in porous media. *Journal of Computational  
1109 Physics*, 337, 275–288. doi: 10.1016/j.jcp.2017.02.041
- 1110 Wang, N., Zhang, D., Chang, H., & Li, H. (2020). Deep learning of subsurface flow  
1111 via theory-guided neural network. *Journal of Hydrology*, 584, 124700. doi: 10  
1112 .1016/j.jhydrol.2020.124700
- 1113 Wang, Y., & Lin, G. (2020). Efficient deep learning techniques for multiphase flow  
1114 simulation in heterogeneous porous media. *Journal of Computational Physics*,  
1115 401, 108968. doi: 10.1016/j.jcp.2019.108968
- 1116 Wen, G., Hay, C., & Benson, S. M. (2021). CCSNet: A deep learning modeling suite  
1117 for CO<sub>2</sub> storage. *Advances in Water Resources*, 155, 104009. doi: 10.1016/j  
1118 .advwatres.2021.104009
- 1119 Wen, G., Li, Z., Azizzadenesheli, K., Anandkumar, A., & Benson, S. M. (2022).  
1120 U-FNO—an enhanced fourier neural operator-based deep-learning model  
1121 for multiphase flow. *Advances in Water Resources*, 163, 104180. doi:  
1122 10.1016/j.advwatres.2022.104180
- 1123 Wen, G., Li, Z., Long, Q., Azizzadenesheli, K., Anandkumar, A., & Benson, S. M.  
1124 (2023). Real-time high-resolution CO<sub>2</sub> geological storage prediction using  
1125 nested fourier neural operators. *Energy & Environmental Science*, 16(4),  
1126 1732–1741. doi: 10.1039/D2EE04204E
- 1127 Wen, G., Tang, M., & Benson, S. M. (2021). Towards a predictor for CO<sub>2</sub> plume mi-  
1128 gration using deep neural networks. *International Journal of Greenhouse Gas  
1129 Control*, 105, 103223. doi: 10.1016/j.ijggc.2020.103223
- 1130 Willard, J., Jia, X., Xu, S., Steinbach, M., & Kumar, V. (2022, November). In-  
1131 tegrating Scientific Knowledge with Machine Learning for Engineering and  
1132 Environmental Systems. *ACM Computing Surveys*, 55(4), 66:1–66:37. doi:  
1133 10.1145/3514228
- 1134 Wu, H., Hu, T., Luo, H., Wang, J., & Long, M. (2023). *Solving high-dimensional  
1135 pdes with latent spectral models*.
- 1136 Wu, Y., & He, K. (2018, September). Group normalization. In *Proceedings of the eu-  
1137 ropean conference on computer vision (eccv)* (pp. 3–19).
- 1138 Xiong, W., Huang, X., Zhang, Z., Deng, R., Sun, P., & Tian, Y. (2023). *Koop-*

- 1139 man neural operator as a mesh-free solver of non-linear partial differential  
1140 equations.
- 1141 Yan, B., Harp, D. R., Chen, B., Hoteit, H., & Pawar, R. J. (2022). A gradient-  
1142 based deep neural network model for simulating multiphase flow in porous  
1143 media. *Journal of Computational Physics*, *463*, 111277. doi: 10.1016/  
1144 j.jcp.2022.111277
- 1145 Yan, B., Harp, D. R., Chen, B., & Pawar, R. (2022). A physics-constrained deep  
1146 learning model for simulating multiphase flow in 3d heterogeneous porous  
1147 media. *Fuel*, *313*, 122693. doi: 10.1016/j.fuel.2021.122693
- 1148 Zheng, F., Jahandideh, A., Jha, B., & Jafarpour, B. (2021). Geologic CO<sub>2</sub> storage  
1149 optimization under geomechanical risk using coupled-physics models. *International  
1150 Journal of Greenhouse Gas Control*, *110*, 103385. doi: 10.1016/j.ijggc  
1151 .2021.103385
- 1152 Zheng, F., Jha, B., & Jafarpour, B. (2022). Optimization of CO<sub>2</sub> storage and leak-  
1153 age through caprock fracturing using coupled flow-geomechanics-fracturing  
1154 simulation. *ECMOR 2022*, *2022*(1), 1–16.
- 1155 Zhu, Y., & Zabaras, N. (2018). Bayesian deep convolutional encoder-decoder net-  
1156 works for surrogate modeling and uncertainty quantification. *Journal of Com-  
1157 putational Physics*, *366*, 415–447. doi: 10.1016/j.jcp.2018.04.018